Geophys. J. Int. (2001) **145,** 77–96

Even-degree lateral variations in the Earth's mantle constrained by free oscillations and the free-air gravity anomaly

Miaki Ishii and Jeroen Tromp*

Department of Earth and Planetary Sciences, Harvard University, 20 *Oxford Street, Cambridge,* MA 02138*, USA.*
E-mail: ishii@seismology.harvard.edu

Accepted 2000 September 21. Received 2000 June 7; in original form 1999 November 16

SUMMARY

The recent occurrence of several large earthquakes, in particular the 1994 June 9 Bolivia event, has motivated a re-examination of the Earth's large-scale heterogeneity from a normal-mode or free-oscillation perspective. Compared to earlier studies, the number of normal-mode constraints on lateral variations in the mantle has increased five-fold, and toroidal and cross-coupled modes complement the traditional spheroidal mode data set. It is demonstrated that this large collection of mode data, combined with the free-air gravity anomaly, can reliably constrain even-degree lateral variations in wave velocities as well as density. We present the first whole-mantle density model constrained by seismology. Our shear and compressional velocity models are consistent with existing models based upon traveltimes and waveforms, and are reasonably well correlated throughout the mantle. Shear and bulk sound velocity models exhibit a gradual decrease in correlation with depth, and are anti-correlated near the core–mantle boundary. We find that lateral variations in density are poorly correlated with wave velocities, and are locally anti-correlated with shear velocity in the lowermost mantle. The correlations between wave velocities and density suggest both a thermal and a compositional origin to lateral heterogeneity. In addition to traditional maps of lateral variations in wave velocity, we also present maps of lateral variations in shear and bulk moduli. The inversion puts weak constraints on even-degree topographic variations on the core–mantle boundary, the 660 km discontinuity and dynamic free surface topography. Finally, we determine both radially and laterally varying scaling relationships, including Poisson's ratio.

Key words: density, free-air gravity, free oscillations, Poisson's ratio, seismic tomography, seismic velocities.

1 INTRODUCTION

Mantle convection, the engine of plate tectonics, is driven by density heterogeneities inside the Earth. One of the manifestations of mantle convection is the anomalous gravity field observed at the Earth's surface, which may be used to estimate the viscosity profile within the mantle. Currently, a mantle density model is constructed from a seismic velocity model under the assumption that variations in velocity can be simply related to variations in density. Such relationships have been determined from mineral physics (Anderson *et al.* 1968; Anderson 1987, 1989; Karato 1993). Predictions of the gravity field based upon scaled velocity models have been quite successful (e.g. Hager & Clayton 1989). However, the assumption of a simple relationship between velocity and density is questionable when lateral variations are a result of non-thermal effects, and studies have indicated that the anomalies may be due, in part, to compositional variations (Forte *et al.* 1995; Masters *et al.* 2000). An independently constrained 3-D density model is required to avoid mapping the uncertainty introduced by scaling seismic velocity models into model parameters such as the radial viscosity profile.

Attempts to determine the density structure of the mantle have been made using the history of plate motions and subducted slabs (Ricard *et al.* 1993; Lithgow-Bertelloni & Richards 1998). Determination of a density model has relied on such an indirect method because body waves are not directly sensitive to variations in density. Using surface waves, Tanimoto (1991) determined an upper mantle density model that has strong high-degree components.

* Now at: Seismological Laboratory, California Institute of Technology, Mail Code 252-21, Pasadena, CA 91125, USA.

Free oscillations, unlike body waves, are sensitive to the density distribution in the entire mantle because the gravitational restoring force is important for long-period waves. Despite this theoretical sensitivity, earlier normal-mode studies considered only lateral variations in shear velocity, under the assumption that variations in compressional velocity and density are related to shear velocity structure by a constant or depth-dependent scaling relationship (Ritzwoller *et al.* 1988; Li *et al.* 1991). Using the new data set, this assumption can be avoided and we invert for independent 3-D models of velocity and density or shear modulus, bulk modulus and density. From these models we derive depth-dependent and 3-D scaling relationships.

Because normal modes are a result of the constructive interference of waves travelling in opposite directions around the globe, they are mainly sensitive to even-degree structure, since the odd degrees average out. Coupled modes give some sensitivity to odd-degree structure, but analysis of these modes has begun only recently (Resovsky & Ritzwoller 1995, 1998), and the number of odd-degree coefficients is not yet sufficient to place a strong constraint on the odd-degree structure of the Earth. Therefore, we will focus only on the even-degree part of the Earth's heterogeneity in this paper.

Normal-mode inversions for the density structure of the mantle are controversial. Some argue that the available data set is still of insufficient quality for the determination of an independent density model (Masters *et al.* 2000a,b). Others believe the inversions are sensitive to the starting model (Resovsky & Ritzwoller 1999b), or see strong trade-offs between density and velocity structure (Kuo & Romanowicz 1999). We have attempted to address all of these issues in this paper, and present what we believe to be the best-constrained 3-D density model based upon current methods and data sets.

2 THEORY

2.1 Parametrization

Isotropic material properties can be described by three independent parameters. One may use variations in shear velocity (β), compressional velocity (α) and density (ρ), which is a natural choice when analysing the seismic properties of the mantle or when the data consist of shear or compressional traveltime observations. On the other hand, to investigate the properties of mantle minerals it is more informative to use variations in rigidity or shear modulus (μ), isentropic incompressibility or adiabatic bulk modulus (κ) and density. These two sets of parametrizations of an isotropic material are related by $\beta^2=\mu/\rho$ and $\alpha^2=(\kappa+4\mu/3)/\rho$. We perform inversions with the 'seismic' parametrization in terms of β, α and ρ, and compare the results with inversions using the 'mineralogical' parametrization in terms of μ, κ and ρ. Earth models resulting from inversions for seismic parameters are named 'S6e', 'SP6e' or 'SPRD6e', whereas those for mineralogical parameters are denoted by 'M6e', 'MK6e' or 'MKRD6e'. A third and final parametrization involves shear velocity β, bulk sound velocity $\gamma=\sqrt{\kappa/\rho}$ and density ρ, which results in models identified by 'SB6e' or 'SBRD6e'.

The number of model parameters in the inversion can be reduced by assuming a simple scaling relationship between different parameters. For example, variations in density may be obtained by scaling a shear velocity model with a factor v_ρ, such that $\delta\ln\rho=v_\rho\delta\ln\beta$. Scaling factors are generally obtained from mineral physics experiments (e.g. Anderson *et al.* 1968; Anderson 1987, 1989) and theoretical calculations (e.g. Karato 1993), by fitting geoid observations using seismic velocity models (e.g. Forte *et al.* 1994) or by comparing shear (S) and compressional (P) velocity models (e.g. Dziewonski & Woodhouse 1987). Typical values are 0.55 to obtain a compressional velocity model from a shear velocity model (v_α), 0.2 to obtain density from shear velocity (v_ρ), and 0.5 for converting shear velocity into bulk modulus (v_κ). These scaling assumptions are valid if the lateral variations have a single cause that affects all model parameters in the same way. Lateral variations in temperature give rise to one such mechanism: as temperature increases, the values of seismic velocities and density decrease. However, there may be non-thermal sources of heterogeneity such as chemical variations, in which case models may not be related by a scaling relationship.

2.2 Splitting function

The splitting of a mode or coupled pair of modes can be visualized in the form of a splitting function (Giardini *et al.* 1987),

$$\sigma(\hat{\mathbf{r}})=\sum_{s=0}\sum_{t=-s}^{s} c_{st}\,Y_{st}(\hat{\mathbf{r}})\,,$$

where $\hat{\mathbf{r}}$ denotes points on the unit sphere and Y_{st} are fully normalized spherical harmonics of degree s and order t (Edmonds 1960). Each mode or mode pair has its own unique splitting function, which represents a local radial average of the Earth's 3-D structure. For isolated modes at high degrees, the splitting function is equivalent to a surface wave phase velocity map. Isolated modes are only sensitive to even-degree heterogeneity since the odd-degree signal is cancelled out by destructive interference of travelling waves. In principle, coupled modes give further constraints on even-degree structure and add valuable constraints on the odd degrees. However, the analysis of coupled modes is in its infancy (Resovsky & Ritzwoller 1995, 1998), and we consider only even degrees in this study.

The spherical harmonic coefficients of the splitting function, c_{st}, are linearly related to 3-D relative variations in the seismic parameters shear velocity $\delta\beta/\beta$, compressional velocity $\delta\alpha/\alpha$ and density $\delta\rho/\rho$ and normalized topography on various boundaries $\delta d/a$ by (Woodhouse & Dahlen 1978; Dahlen & Tromp 1998)

$$c_{st}=\int_b^a \left[(\delta\beta/\beta)_{st}\,K_s^\beta+(\delta\alpha/\alpha)_{st}\,K_s^\alpha+(\delta\rho/\rho)_{st}\,K_s^\rho\right]dr + \sum_d (\delta d/a)_{st}\,K_s^d\,. \quad (1)$$

Since only modes sensitive to the mantle are used in this study, the integration is from the core–mantle boundary (CMB) with radius b to the Earth's surface with radius a. The summation is over all discontinuities, which include the free surface, the 410 km discontinuity, the 660 km discontinuity and the CMB. The sensitivity kernels are calculated using spherically symmetric earth model PREM (Dziewonski & Anderson 1981). They are dependent upon the spherical harmonic degree s but not upon the order t and are defined in terms of the eigenfunctions of the mode (Woodhouse 1980; Li *et al.* 1991).

Eq. (1) can be rewritten in terms of relative perturbations in the mineralogical parameters shear modulus $\delta\mu/\mu$, bulk modulus $\delta\kappa/\kappa$ and density $\delta\rho/\rho$ as

$$c_{st} = \int_b^a \left[(\delta\mu/\mu)_{st}\, K_s^\mu + (\delta\kappa/\kappa)_{st}\, K_s^\kappa + (\delta\rho/\rho)_{st}\, K_s^\rho\right] dr + \sum_d (\delta d/a)_{st}\, K_s^d\,, \tag{2}$$

or in terms of relative perturbations in shear velocity $\delta\beta/\beta$, bulk sound velocity $\delta\gamma/\gamma$ and density $\delta\rho/\rho$ as

$$c_{st} = \int_b^a \left[(\delta\beta/\beta)_{st}\, K_s^\beta + (\delta\gamma/\gamma)_{st}\, K_s^\gamma + (\delta\rho/\rho)_{st}\, K_s^\rho\right] dr + \sum_d (\delta d/a)_{st}\, K_s^d\,. \tag{3}$$

We use all three representations, eqs (1), (2) and (3), in our inversions.

Due to a lack of data, previous normal-mode studies reduced the number of unknown parameters by neglecting the effects of boundary topography and by relating different models through scaling factors. For example, if relative variations in density are related to relative variations in shear velocity by a scaling factor v_ρ, such that $\delta\ln\rho = v_\rho\delta\ln\beta$, and compressional and shear velocity are related by another scaling factor v_α, $\delta\ln\alpha = v_\alpha\delta\ln\beta$, then eq. (1) reduces to

$$c_{st} = \int_b^a \left[(\delta\beta/\beta)_{st}\, {}^\star K_s^\beta\right] dr\,, \tag{4}$$

where ${}^\star K_s^\beta = K_s^\beta + v_\alpha K_s^\alpha + v_\rho K_s^\rho$. This approach has been used recently by Resovsky & Ritzwoller (1999a) to obtain a degree 8 mantle shear velocity model.

2.3 Free-air gravity anomaly

The perturbed gravitational potential, $\delta\Phi$, satisfies Poisson's equation,

$$\nabla^2\delta\Phi = 4\pi G\,\delta\rho\,,$$

where G is the gravitational constant and $\delta\rho$ denotes variations in density. Solving Poisson's equation, we obtain

$$\delta\Phi(\mathbf{r}) = -G\int_V \frac{\delta\rho(\mathbf{r}')}{|\mathbf{r}-\mathbf{r}'|}\, d^3\mathbf{r}' + G\sum_d \int_S \frac{[\rho]_-^+\delta d(\hat{\mathbf{r}}')}{|\mathbf{r}-\mathbf{r}'|}\, d^2\mathbf{r}'\,,$$

where $\mathbf{r}$ denotes the position vector, $[\rho]_-^+$ is the density jump at a discontinuity d, and δd is the topography on that discontinuity. Using the relationship (Forte & Peltier 1987; Dahlen & Tromp 1998)

$$\frac{1}{|\mathbf{r}-\mathbf{r}'|} = \sum_{s=0}^{\infty}\frac{4\pi}{2s+1}\,\frac{[\min(r,r')]^s}{[\max(r,r')]^{(s+1)}}\sum_{t=-s}^{s} Y_{st}(\hat{\mathbf{r}})\,Y_{st}^*(\hat{\mathbf{r}}')\,,$$

where $\mathbf{r} = r\hat{\mathbf{r}}$ defines the radius r, and expanding $\delta\rho$, δd and $\delta\Phi$ in spherical harmonics as

$$\delta\rho(\mathbf{r}') = \sum_{s,t}\delta\rho_{st}(r')\,Y_{st}(\hat{\mathbf{r}}')\,,\qquad \delta d(\hat{\mathbf{r}}') = \sum_{s,t}\delta d_{st}\,Y_{st}(\hat{\mathbf{r}}')\,,$$

$$\delta\Phi(\mathbf{r}') = \sum_{s,t}\delta\Phi_{st}(r')\,Y_{st}(\hat{\mathbf{r}}')\,,$$

we obtain the following expression for the spherical harmonic coefficients of the gravitational potential at the Earth's surface with radius a:

$$\delta\Phi_{st}(a) = -\frac{4\pi G}{2s+1}\int_b^a \delta\rho_{st}(r)\,\frac{r^s}{a^{s+1}}\,r^2 dr + \frac{4\pi G}{2s+1}\sum_d [\rho]_-^+\frac{d^{s+2}}{a^{s+1}}\,\delta d_{st}\,.$$

In this study we use the free-air gravity anomaly rather than the gravitational potential, because the former has whiter spectrum than the latter, which is dominated by degree 2. The free-air gravity anomaly coefficients f_{st} are related to the gravitational potential coefficients $\delta\Phi_{st}$ by

$$f_{st}(a) = -\frac{3g(s-1)}{4\pi a^2 G\bar{\rho}}\,\delta\Phi_{st}(a)\,,$$

where g is the gravitational acceleration at the Earth's surface and $\bar{\rho}$ is the average density of the Earth. This allows us to write the relationship between the free-air gravity coefficients and the relative variations in density and boundary topography in a linear equation much like eq. (1),

$$f_{st} = \int_b^a (\delta\rho/\rho)_{st}\, K_s'^{\rho}\, dr + \sum_d (\delta d/a)_{st}\, K_s'^{d}\,, \tag{5}$$

where $K_s'^{\rho}$ and $K_s'^{d}$ are the density and discontinuity sensitivity kernels of the free-air gravity anomaly given, respectively, by

$$K_s'^{\rho} = -\frac{3g(s-1)}{2s+1}\,(\rho/\bar{\rho})\left(\frac{r^s}{a^{s+1}}\right),$$

$$K_s'^{d} = \frac{3g(s-1)}{2s+1}\,[\rho/\bar{\rho}]_-^+\left(\frac{d}{a}\right)^{s+2}.$$

Note that our gravity modelling is based upon a static approach that does not require knowledge of the viscous structure of the mantle. We invert directly for lateral variations in density and boundary topography, which is sufficient for predictions of the gravity anomaly; no viscous flow calculation or velocity-to-density scaling are required.

3 FORMULATION OF THE INVERSE PROBLEM

A general 3-D model of the mantle, $\delta m/m$, is expanded laterally in spherical harmonics and radially in Chebyshev polynomials as follows:

$$\delta m/m(\mathbf{r}) = \sum_{n=0}^{n_{\max}}\sum_{s=0}^{s_{\max}}\sum_{t=-s}^{s} {}_n(\delta m/m)_{st}\, T_n(r)\, Y_{st}(\hat{\mathbf{r}})\,,$$

where $n_{\max}$ is the maximum radial order of the Chebyshev polynomials T_n, and $s_{\max}$ is the maximum spherical harmonic degree. In our inversion we use $n_{\max} = 13$ and $s_{\max} = 6$. We use the renormalized Chebyshev polynomials defined by Su (1992). To investigate the effects of radial parametrization on the final model, we will also briefly consider a radial b-spline basis.

Using this general expansion, we define a combined M-dimensional model vector $\mathbf{m}$ by

$$\mathbf{m} = \left[{}_n(\delta\beta/\beta)_{st}\;\; {}_n(\delta\alpha/\alpha)_{st}\;\; {}_n(\delta\rho/\rho)_{st}\;\; (\delta d/a)_{st}\right]^{\mathrm{T}},$$

where T denotes the transpose. Similarly, we define an N-dimensional data vector $\mathbf{d}$ containing the N_s splitting function coefficients and N_f free-air gravity anomaly coefficients, such that $N = N_s + N_f$, by

$$\mathbf{d} = [\,{}_k c_{st} \;\; f_{st}\,]^T ,$$

where the subscript k is used as a mode or mode-pair label. Using eqs (1), (2) or (3) together with eq. (5), the linear relationship between the data vector $\mathbf{d}$ and the model vector $\mathbf{m}$ may be written in matrix notation as

$$\mathbf{d} = \mathbf{K}\mathbf{m} ,$$

where $\mathbf{K}$ is a matrix with dimensions $N \times M$. For the seismic parametrization, the matrix $\mathbf{K}$ is defined in terms of the sensitivity kernels by

$$\mathbf{K} = \begin{bmatrix} {}_k K_s^{\beta} & {}_k K_s^{\alpha} & {}_k K_s^{\rho} & {}_k K_s^{d} \\ 0 & 0 & K_s'^{\rho} & K_s'^{d} \end{bmatrix} .$$

We seek to determine the model vector that minimizes the objective function

$$f(\mathbf{m}) = [\mathbf{d} - \mathbf{K}\mathbf{m}]^T \mathbf{W} [\mathbf{d} - \mathbf{K}\mathbf{m}] + [\mathbf{m} - \mathbf{m}_0]^T \mathbf{D} [\mathbf{m} - \mathbf{m}_0] ,$$

where $\mathbf{W}$ is a square diagonal matrix with dimensions $N \times N$ that assigns a weighting to each datum. The diagonal elements of this matrix are usually $1/\sigma_i^2$, where σ_i is the estimated uncertainty of datum d_i. The purpose of the square $M \times M$ damping matrix $\mathbf{D}$ is to find a model $\mathbf{m}$ that is similar to a starting model represented by the M-dimensional vector $\mathbf{m}_0$. We use a combination of norm, first- and second-derivative damping.

Minimizing the objective function, we obtain

$$\mathbf{m} = \left(\mathbf{K}^T \mathbf{W} \mathbf{K} + \mathbf{D}\right)^{-1} \left(\mathbf{K}^T \mathbf{W} \mathbf{d} + \mathbf{D} \mathbf{m}_0\right).$$

The resolution matrix $\mathbf{R}$ of the inverse problem is given by

$$\mathbf{R} = \left(\mathbf{K}^T \mathbf{W} \mathbf{K} + \mathbf{D}\right)^{-1} \mathbf{K}^T \mathbf{W} \mathbf{K} , \tag{6}$$

and the trace of this matrix, tr($\mathbf{R}$), represents the number of resolved parameters for a given choice of damping. The associated covariance matrix for the model parameters is given by

$$\mathbf{C} = \left(\mathbf{K}^T \mathbf{W} \mathbf{K} + \mathbf{D}\right)^{-1} \mathbf{K}^T \mathbf{W} \mathbf{K} \left(\mathbf{K}^T \mathbf{W} \mathbf{K} + \mathbf{D}\right)^{-1} . \tag{7}$$

The square root of a diagonal element of the covariance matrix $\sqrt{C_{ii}}$ defines the standard error associated with the ith model parameter m_i. However, in a damped least-squares inversion the uncertainty associated with the model parameters is highly dependent upon the damping matrix $\mathbf{D}$ and may not provide a realistic error estimate.

3.1 Robustness tests

There are well-known tests for examining the resolution and uniqueness of a model obtained from an inversion. Statistical tests such as variance reduction and χ^2 tests are most commonly used to determine how well the models fit the data. The effects of damping upon models are investigated with a resolution test. The Backus–Gilbert resolution test (Backus & Gilbert 1968) describes which part of the 'true' Earth structure is mapped into a given portion of the inverted model. We briefly review resolution tests and Backus–Gilbert tests in the next two sections.

3.1.1 *Resolution tests*

Applying damping to an inverse problem reduces the amplitude and smoothes the model. The significance of these effects may be assessed based upon a resolution test. Synthetic data are calculated using a given trial model, and are inverted using the same damping as in the real inversion to investigate the recovery of the trial model. To be realistic, one may add random noise to the synthetic data and run the inversion to gain insight into the effects of noise. In the ideal case, the resulting model is identical to the trial model. However, due to the damping, the inverted model generally is a smoother version of the input model.

The formulation of a resolution test is most easily accomplished by using the resolution matrix $\mathbf{R}$ defined by eq. (6). Expanding the output model $g(\mathbf{r})$ using general basis functions $B_i(\mathbf{r})$, we may write

$$g(\mathbf{r}) = \sum_i g_i B_i(\mathbf{r}) . \tag{8}$$

The expansion coefficients g_i are related to the model coefficients m_j through the resolution matrix: $g_i = \Sigma_j \, R_{ij} m_j$. Substituting this expression for g_i into eq. (8), we find

$$g(\mathbf{r}) = \sum_{i,j} B_i(\mathbf{r}) R_{ij} m_j . \tag{9}$$

We perform two types of resolution tests. The first type of test involves an input model that consists of only one non-zero value for a specific radial order n, angular degree s and angular order t. This is equivalent to studying the response of the inversion to a delta-function perturbation in the wavenumber domain. The second type of test involves an input model which is a delta-function in a mixed domain: a model with specific angular degree s and order t peaked at a given depth. This type of test examines the radial smearing due to damping.

3.1.2 *Backus–Gilbert resolution tests*

In contrast to the resolution test, which investigates how a given model is affected by the inversion, a Backus–Gilbert resolution test asks how an inverted model is related to the 'true' earth model. Let $g(\mathbf{r}')$ be the model obtained from an inversion at a given position $\mathbf{r}'$ and let $m(\mathbf{r})$ be the 'true' earth model. Then the Backus–Gilbert resolution kernel is an averaging kernel $A(\mathbf{r}', \mathbf{r})$ relating the inverted and 'true' earth models (Backus & Gilbert 1968),

$$g(\mathbf{r}') = \int A(\mathbf{r}', \mathbf{r}) m(\mathbf{r}) d^3\mathbf{r} . \tag{10}$$

In the ideal case where $g(\mathbf{r}') = m(\mathbf{r}')$, the Backus–Gilbert resolution kernel is a Dirac-delta function: $A(\mathbf{r}', \mathbf{r}) = \delta(\mathbf{r} - \mathbf{r}')$.

Expanding $m(\mathbf{r})$ in radial basis functions $B_i(\mathbf{r})$, and using the orthogonality of the basis functions $\int w(\mathbf{r}) B_i^*(\mathbf{r}) B_j(\mathbf{r}) d^3\mathbf{r} = \delta_{ij}$, where an asterisk denotes complex conjugation and $w(\mathbf{r})$ is a weighting function, we can write

$$m_j = \int m(\mathbf{r}) w(\mathbf{r}) B_j^*(\mathbf{r}) d^3\mathbf{r} .$$

Combining this expression with eq. (9), we obtain

$$g(\mathbf{r}') = \int \sum_{i,j} w(\mathbf{r}) B_i(\mathbf{r}') R_{ij} B_j^*(\mathbf{r}) m(\mathbf{r}) d^3\mathbf{r} .$$

Upon comparing the last equation with eq. (10) we deduce that the Backus–Gilbert resolution kernel is given in terms of the resolution matrix and the basis functions by

$$A(\mathbf{r}', \mathbf{r}) = \sum_{i,j} w(\mathbf{r}) B_i(\mathbf{r}') R_{ij} B_j^*(\mathbf{r}) .$$

Generally, Backus–Gilbert resolution tests are used to determine the averaging in the radial direction. Therefore, Backus–Gilbert kernels are often calculated for specific values of the angular degree s and order t, and the resulting kernel is plotted as a function of depth.

4 DATA

In earlier normal-mode studies (Giardini *et al.* 1987; Ritzwoller *et al.* 1988; Li *et al.* 1991), splitting function coefficients of very long-period, isolated spheroidal modes were determined for degrees 2 and 4 (Giardini *et al.* 1987, 1988; Ritzwoller *et al.* 1988). The occurrence of several large earthquakes in 1994–1996 has motivated new normal-mode studies, and as a result the quality and quantity of splitting function coefficients have improved dramatically. Compared to earlier data sets, higher-degree coefficients corresponding to smaller-scale structures have been measured up to angular degree and order 12 (Ritzwoller & Resovsky 1995; He & Tromp 1996; Resovsky & Ritzwoller 1998). We use even-degree splitting function coefficients up to and including spherical harmonic degree 6. Splitting coefficients of many modes are available up to this degree and we believe that there are not enough coefficients above degree 6 to reliably constrain 3-D mantle heterogeneity. Another improvement to the data set comes from the addition of isolated toroidal modes (Tromp & Zanzerkia 1995; Resovsky & Ritzwoller 1998). These modes provide valuable additional constraints on shear velocity structure. Our data set consists of 2850 even-degree splitting function coefficients from 126 spheroidal, 42 toroidal and 16 cross-coupled modes; consequently, our 3-D mantle models consist only of even degrees.

There is an overlap in data sets determined by different groups. We include estimates from various groups as independent constraints, much like using multiple rays passing through the same region in body wave tomography. In general, data from different groups are reasonably consistent (Fig. 1). Nevertheless, we also performed inversions with a data set in which the measurements and their associated error estimates were averaged. The models were virtually identical to those based upon the data set with multiple measurements. Similarly, we performed two inversions, one based only upon the Resovsky & Ritzwoller (1998) data set and the other based upon the He & Tromp (1996) data set. Again, the consistency of the resulting models was statistically significant, as discussed further in Section 6.

Besides the splitting functions, the free-air gravity anomaly is included in our data set. This provides important additional constraints because it is uniquely sensitive to density and boundary topography. We use geopotential model EGM96 (Lemoine *et al.* 1997, 1998a,b) and make a hydrostatic correction (Nakiboglu 1982). The geopotential coefficients are subsequently converted to free-air gravity coefficients. The gravity anomaly coefficients are only included in the data set when the inversion includes lateral variations in density and boundary topography.

5 MODELS

5.1 Corrections and starting models

Before the data can be inverted for velocity and density models of the mantle, effects due to the crust must be removed. This correction is calculated using recent crustal model Crust5.1 (Mooney *et al.* 1998). For the free-air gravity anomaly, we assume that the crust is isostatically compensated, which gives a small contribution to the Earth's gravity field. We have performed inversions with and without this correction for gravity and confirmed that it is negligible, as assumed in (Ishii & Tromp 1999). We make no further corrections to the free-air gravity anomaly, such as a lithospheric correction; therefore, our 'dynamic topography' is the non-isostatic topography of the free surface that is produced by density anomalies within the entire mantle.

We seek even-degree models of shear (S) velocity, compressional (P) velocity, density, dynamic topography on the free surface, and topography on the 660 km discontinuity (660) and the CMB. To take advantage of models based mainly upon traveltime and waveform data, we use such models as starting models in our inversions. We choose S-velocity model SKS12WM13 (Dziewonski *et al.* 1997), P-velocity model P16B30 (Bolton 1996), and the 660 model of Gu *et al.* (1998) as our starting models. For a density starting model we use SKS12WM13 scaled by a factor of 0.2. The free surface and the CMB have zero starting topography. However, we use the excess ellipticity of the CMB determined by very long baseline interferometry (Gwinn *et al.* 1986). Initially, we inverted for topography on the 410 km discontinuity (410) but found that this boundary is not well resolved by our data, presumably because it is dominated by degree 1 heterogeneity (Gu *et al.* 1998; Flanagan & Shearer 1998). Therefore, a model of topographic variations on 410 by Gu *et al.* (1998) is used to calculate a correction due to this boundary.

This set of starting models with crustal and 410 corrections explains 74 per cent of variance in the even-degree splitting functions, which translates into a χ^2/N_e of 6.6, where $N_e = 2850$ is the number of even-degree splitting function coefficients. Damping parameters are chosen in the inversions such that these are stable and result in reasonably smooth models. Throughout our experiments, the same damping was applied to S and P velocity, and the damping of the density model was required to be the same as, or slightly greater than, that of the velocity models.

5.2 3-D models

Assuming that the scaling relationships between models are valid, i.e. $\delta\ln\alpha = 0.55\delta\ln\beta$ and $\delta\ln\rho = 0.2\delta\ln\beta$, we obtain shear velocity model S6e and rigidity model M6e by relating splitting coefficients to shear velocity or rigidity structure as in eq. (4). In Figs 2(a) and (b), mode-by-mode improvements in χ^2/N are illustrated when the fit achieved by model SKS12WM13 is compared to the fit based upon model S6e. Fundamental spheroidal modes ($_0S$ branch), which are sensitive

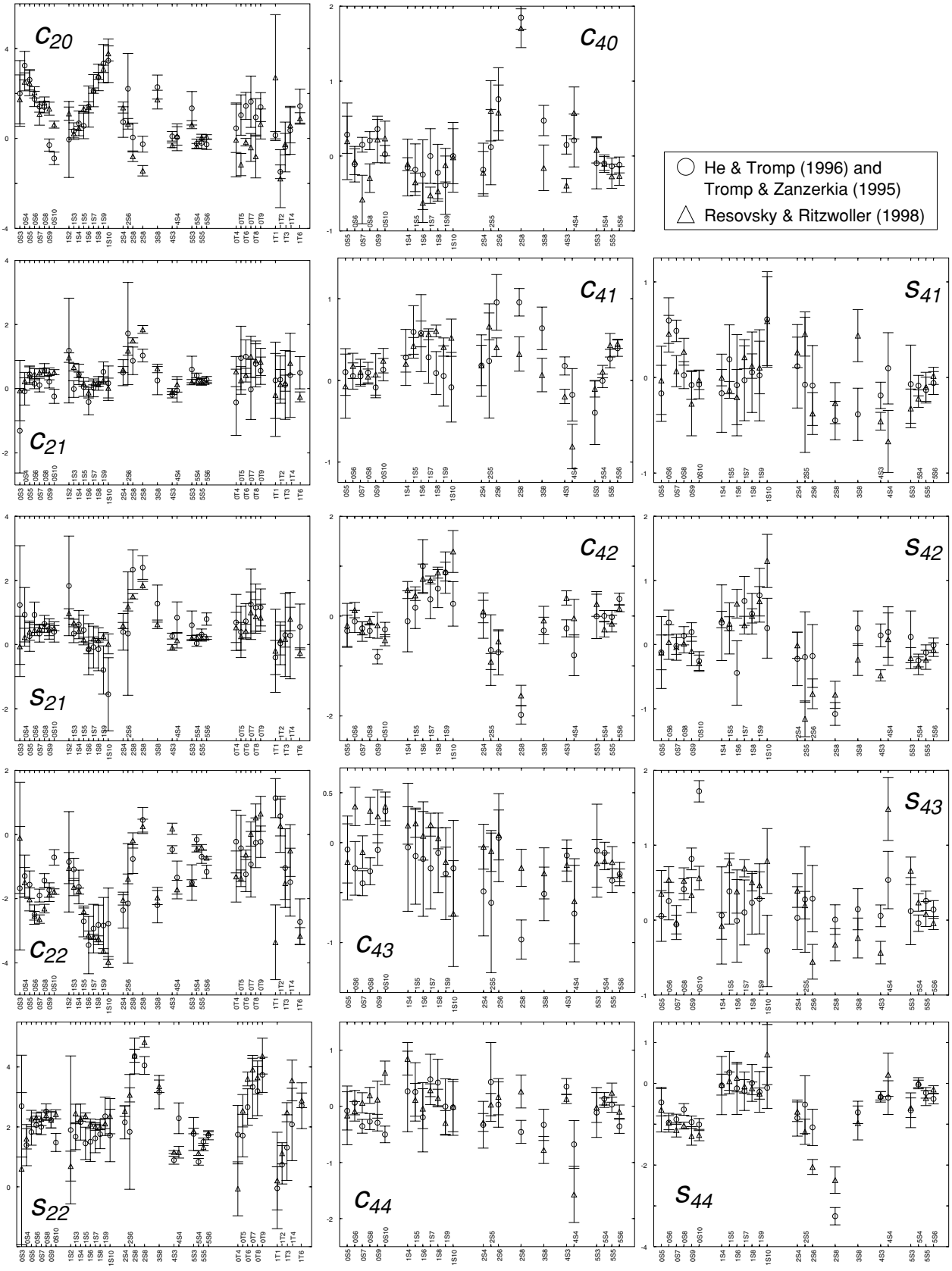

Figure 1. Comparison of splitting function coefficients determined by two different groups. Those denoted by circles are measurements made by He & Tromp (1996) for spheroidal modes and by Tromp & Zanzerkia (1995) for toroidal modes. Measurements shown by triangles were made by Resovsky & Ritzwoller (1998). The coefficients are those of fully normalized spherical harmonics (Edmonds 1960), *c* denotes the real part and *s* denotes the imaginary part; coefficients have been corrected for crustal structure using model Crust5.1 (Mooney *et al.* 1998). In general, there is good agreement between measurements made by different groups.

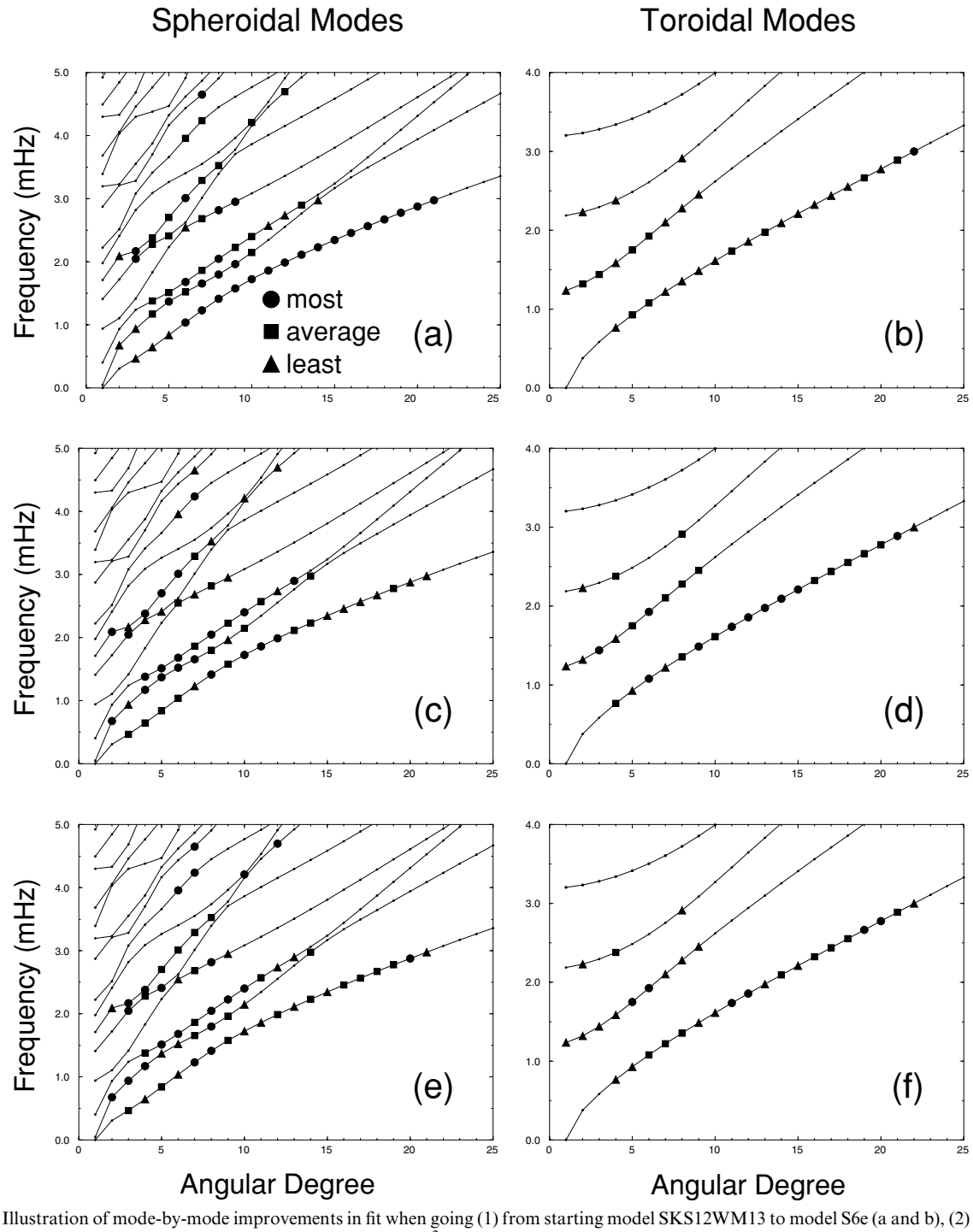

Figure 2. Illustration of mode-by-mode improvements in fit when going (1) from starting model SKS12WM13 to model S6e (a and b), (2) from S6e to SP6e (c and d), and (3) from SP6e to SPRD6e (e and f). We monitor χ^2/N' for each individual toroidal or spheroidal mode, where N' denotes the number of splitting function coefficients for that mode. The modes are binned into three groups of equal size: modes denoted by circles show the most improvement in fit, modes indicated by squares are average, and modes denoted by triangles show the least improvement. (a) Improvements in χ^2/N' for isolated spheroidal modes going from SKS12WM13 to S6e. Fundamental spheroidal modes, which are sensitive to shear velocity structure in the mid- and upper mantle, consistently show large improvements. (b) Same as in (a) but for toroidal modes. Note that the fit to these modes does not improve very much compared to the spheroidal modes. (c) Same as in (a) but for improvements in fit going from S6e to SP6e. Compared to (a), modes with low angular degrees improve in fit when lateral variations in P velocity are added to the inversion. These modes, in particular on the fifth overtone branch, are generally sensitive to P-velocity structure. (d) Same as in (b) but for improvements in fit going from S6e to SP6e. The fundamental toroidal modes show large improvements in fit when independent lateral variations in P velocity are introduced. In model S6e, the S-velocity model is forced to accommodate P-velocity variations as well as S heterogeneity in order to fit the spheroidal modes (many of which have strong sensitivity to P heterogeneity). On the other hand, model SP6e allows for independent variations in S and P velocity such that P-sensitive modes no longer alias P structure into S structure. Hence the S model is available to fit the toroidal modes. (e) Same as in (a) but for improvements in fit going from SP6e to SPRD6e. The low degree, higher-frequency spheroidal modes are most affected; these are the modes with significant sensitivity to density. (f) Same as in (b) but for improvements in fit going from SP6e to SPRD6e. Density heterogeneity does not affect the fit to toroidal modes significantly, which is to be expected.

to shear velocity structure in the mid-mantle, show large improvements, indicating that mid-mantle S heterogeneity in model S6e is different from that in SKS12WM13. Improvements in fit to the toroidal modes are not as obvious as for the spheroidal modes.

In the same manner as for the S6e or M6e inversions, we invert for S and P velocity model SP6e, S and bulk sound velocity model SB6e, and rigidity and incompressibility model MK6e. When independent lateral variations in P velocity are introduced, spheroidal modes of low angular degree show the largest improvements in fit (Fig. 2c). These modes, in particular the fifth overtone branch, are generally more sensitive to P-velocity heterogeneity. Because toroidal modes do not have any sensitivity to P velocity, it is counterintuitive to see improvements in fit to fundamental toroidal modes (Fig. 2d). In model S6e, the S-velocity model is forced to accommodate P-velocity variations as well as S heterogeneity in order to fit the well-determined spheroidal modes, many of which have considerable sensitivity to P structure. On the other hand, model SP6e allows for independent variations in S and P velocity, such that P-sensitive modes no longer alias P structure into S structure. Hence the S model is available to fit the toroidal modes.

The improvements in fit going from SP6e to SPRD6e, an inversion involving S velocity, P velocity, density and boundary topography, which includes the free-air gravity anomaly data set, are most evident in the low-degree, higher-frequency spheroidal modes with significant sensitivity to density (Fig. 2e). In contrast, allowing for independent variations in density and topography does not affect the fit to toroidal modes significantly (Fig. 2f). The statistical results of the different inversions and parametrizations are summarized in Table 1.

Because individual models do not vary significantly with changes in the number of model parameters (for example, the S-velocity model from S6e is virtually identical to that of SB6e), we shall focus our discussion on models SPRD6e, MKRD6e and SBRD6e. We observe that these three models, obtained from different inversions, are compatible with one another. As an example, we compare the density models obtained from the three inversions for SPRD6e, MKRD6e and SBRD6e in Fig. 3. This figure illustrates the consistency of the density models both in pattern and in amplitude. Therefore, in what follows, unless noted otherwise, the S and P velocity, density and discontinuity models are those of SPRD6e, the bulk sound model is that of SBRD6e, and shear and bulk modulus models are from MKRD6e.

Fig. 4 shows map views of our even-degree S-velocity model. It agrees well with the S-velocity model based upon body wave data (the even-degree part of SKS12WM13) in the upper and lowermost mantle with slight differences in the mid-mantle (Fig. 5a). As we noted in Fig. 2(a), the splitting data are quite sensitive to structure in this depth range. The power, or root-mean-square (rms) amplitude, of the models is very similar throughout the mantle (Fig. 5b). Note that the rms amplitude is about half of that of body wave tomographic models such as S12WM13 (Su *et al.* 1994) because we are only considering the even degrees.

Similar observations can be made about the P-velocity parts of SPRD6e and P16B30 (Fig. 6). The two models agree well in the upper and lower mantle but exhibit differences in the mid-mantle (Fig. 7a). In contrast to the correlation between the two

Table 1. Variance reduction, χ^2/N_e, and $\chi^2/(N_e - M_e)$, where $N_e = 2850$ is the number of even-degree data and M_e is the number of even-degree model parameters, for various inversions. For a description of the inversions, see the text (Section 5). By definition, $\chi^2 = \Sigma_i (d_i^{pre} - d_i^{obs})^2/\sigma_i^2$, where d_i^{pre} is the ith datum predicted using the models from the inversion and d_i^{obs} is the observed datum with associated uncertainty σ_i. For a zero model, or null hypothesis, χ^2 becomes $\chi_0^2 = \Sigma_i (d_i^{obs})^2/\sigma_i^2$. Variance reduction is defined as $1 - \chi^2/\chi_0^2$. Ideally, $\chi^2/(N_e - M_e)$ should decrease when M_e is increased, if the additional number of model parameters is warranted by the data. As we discuss in Section 6 and Table 2, we overparametrize our models in radius, therefore $\chi^2/(N_e - M_e)$ does not necessarily improve when the number of model parameters is increased.

Model	VR (per cent)	χ^2/N_e	$\chi^2/(N_e - M_e)$	VR (gravity) (per cent)
S6e	89.4	2.7	3.1	NA
M6e	89.2	2.7	3.1	NA
SP6e	90.3	2.5	3.3	NA
SB6e	90.1	2.5	3.4	NA
MK6e	90.2	2.5	3.3	NA
SPRD6e	92.0	2.0	3.5	95.6
SBRD6e	91.8	2.1	3.6	95.2
MKRD6e	91.9	2.1	3.6	95.3

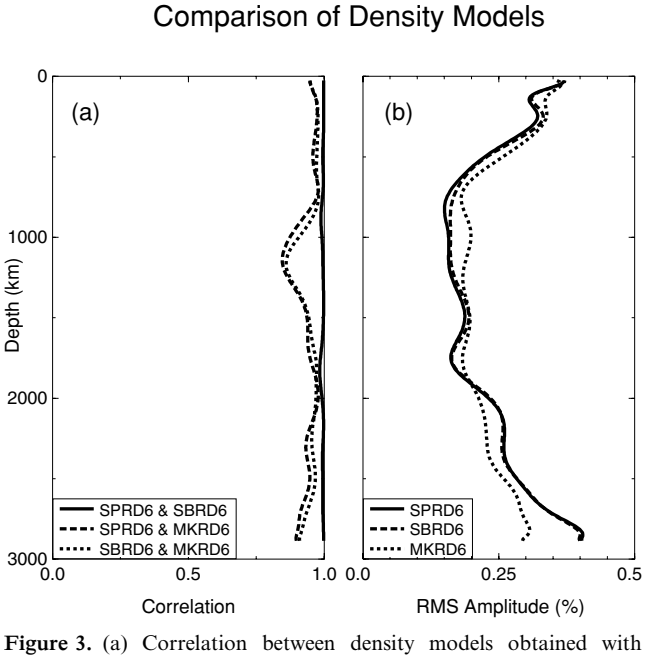

Figure 3. (a) Correlation between density models obtained with different parametrizations. The solid curve is the correlation between the density models of SPRD6e (S velocity, P velocity, density, and boundary topography) and SBRD6e (S velocity, bulk sound velocity, density and boundary topography), the dashed curve is the correlation between SPRD6e and the density part of MKRD6e (rigidity, incompressibility, density and boundary topography) and the dotted curve is the correlation between the density parts of SBRD6e and MKRD6e. The resulting density models are all highly correlated. (b) Rms amplitude of the density part of SPRD6e (solid line), SBRD6e (dashed line) and MKRD6e (dotted line) as a function of depth. The rms values of the three models are similar.

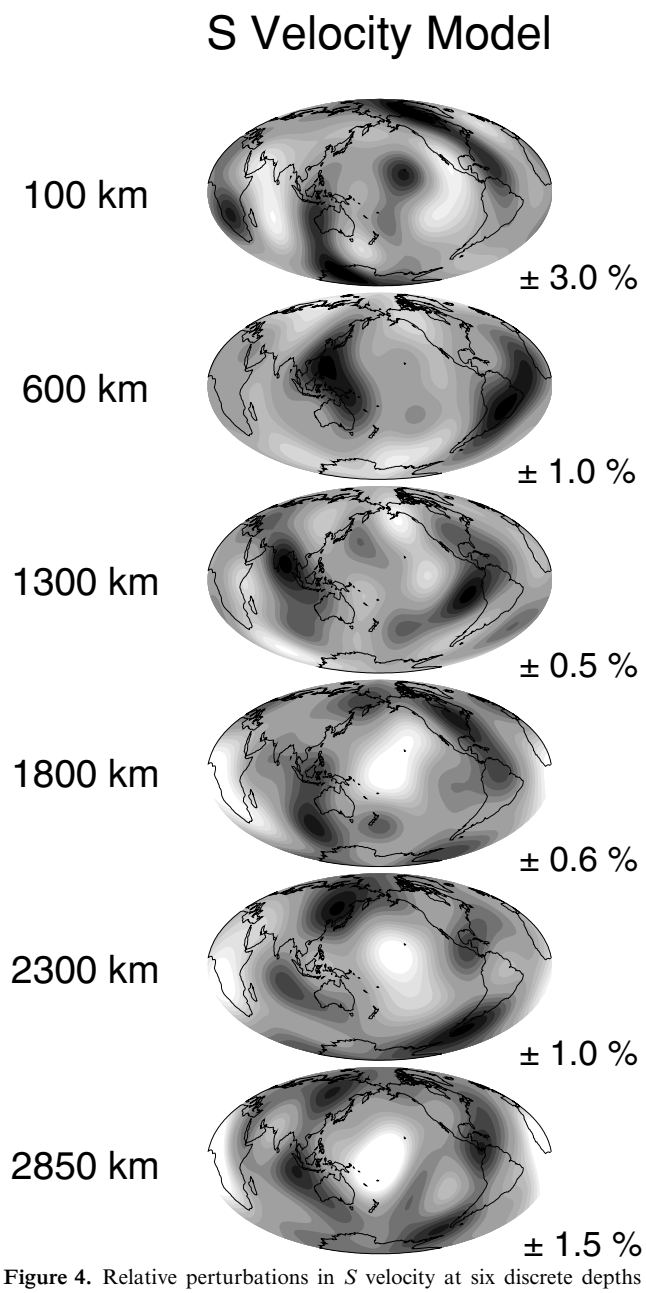

Figure 4. Relative perturbations in S velocity at six discrete depths throughout the mantle (using even-degree coefficients only). Dark shades indicate regions of higher than average velocities and light shades indicate slower than average regions. For each depth, the scale for the maps is indicated. Coastlines have been superimposed for reference.

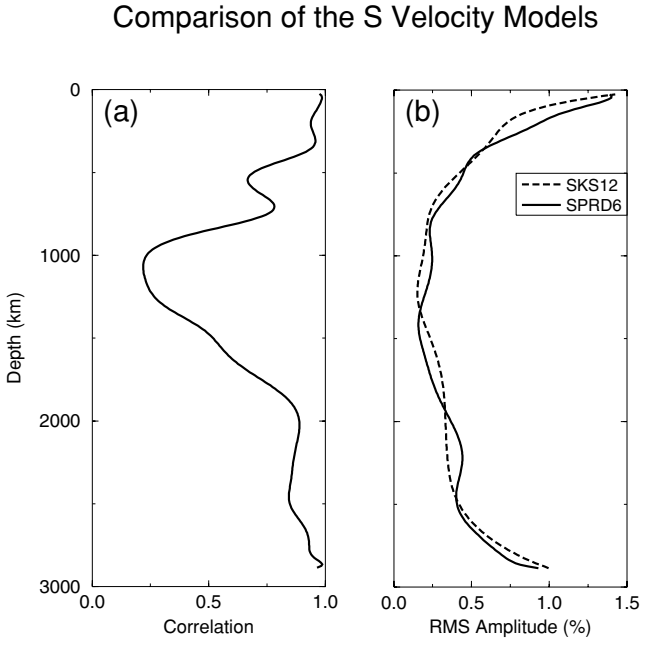

Figure 5. (a) Correlation between the S model of SPRD6e and SKS12WM13 as a function of depth (even-degree coefficients only). Perfectly correlated models have a correlation of 1, de-correlated models have a correlation of 0, and anti-correlated models have a correlation of -1. The 95 per cent significance level for this number of parameters is 0.32. The two S models are well correlated except in the mid-mantle. (b) Rms amplitude of the S part of SPRD6e and SKS12WM13 as a function of depth (even-degree coefficients only). The solid line is SPRD6e and the dashed line is SKS12WM13. The rms amplitudes of the two models are very similar to one another.

S velocity models, the correlation of the P models decreases slightly near the CMB. The rms amplitudes of the models (Fig. 7b) are very similar throughout the mantle, except in the transition zone.

In Fig. 8, the correlation and rms amplitudes of the S and P models are compared. Both models have high amplitudes in the upper mantle and relatively small amplitudes in the mid-mantle. In the lowermost mantle, however, the S-velocity model increases in amplitude near the CMB, whereas the P-velocity model is practically constant throughout the lower mantle. The correlation between the S and P models is high in the upper mantle and around 2500 km depth, but the mid-mantle is characterized by a poorer correlation. Towards the CMB, the correlation also drops, something that has been noted in other studies (Robertson & Woodhouse 1995; Bolton 1996).

In Fig. 9, we plot the bulk sound velocity part of SBRD6e. The most striking feature of the bulk sound velocity model is its anti-correlation with shear velocity in the lowermost mantle. This strong anti-correlation is consistent with other studies where shear and bulk sound velocity models are constrained by S and P traveltime and waveform data (Su & Dziewonski 1997; Masters *et al.* 1999). The correlation between shear and bulk sound velocity models is generally poor, with significant negative values near the CMB (Fig. 10a). Compared to the S-velocity model, the rms amplitude of bulk sound velocity is smaller near the surface and the CMB, but similar in the mid-mantle (Fig. 10b).

The rigidity (μ) and incompressibility (κ) models are shown side by side in Fig. 11. These models cannot be determined based upon traditional traveltime studies, and, despite their direct implications for mantle mineralogy, have not been obtained previously. The two models of μ and κ are significantly anti-correlated near the CMB (Fig. 12a). Note that the amplitude of the heterogeneity is much larger for the μ model than for the wave velocity models (Fig. 12b). This is an expected result since perturbation in rigidity $\delta\mu/\mu$ is related to the S-velocity perturbation $\delta\beta/\beta$ as $\delta\mu/\mu = 2(\delta\beta/\beta) + \delta\rho/\rho$. Because lateral variations in density are small, the correlations between

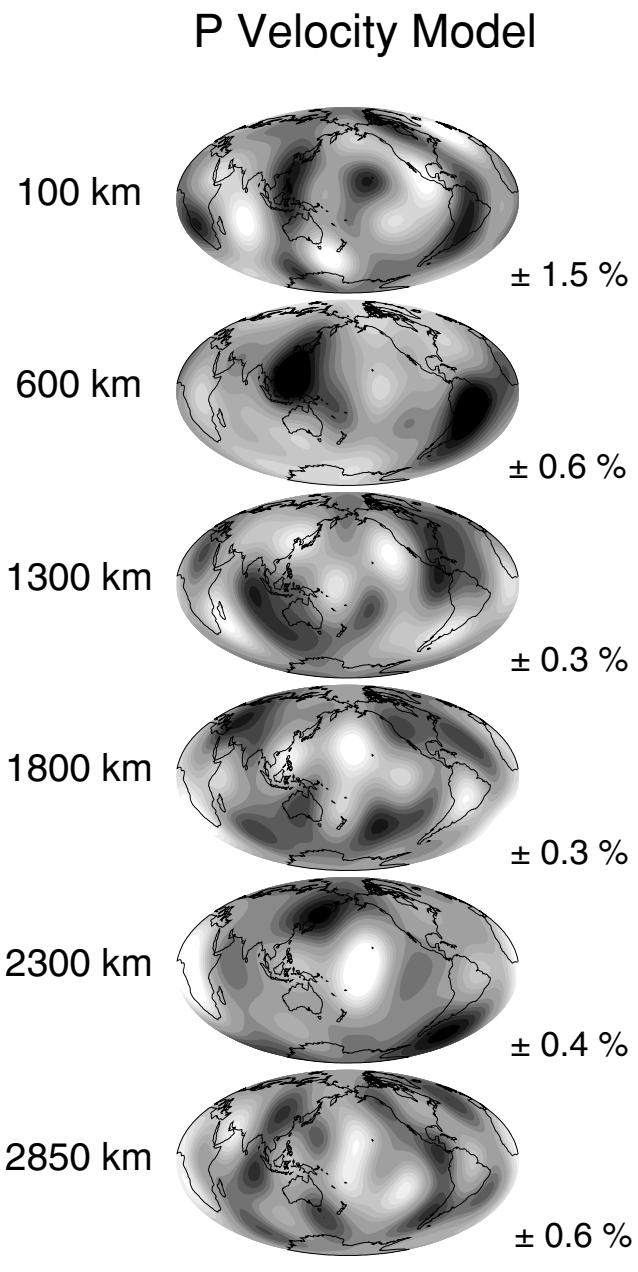

Figure 6. Relative perturbations in *P* velocity at six discrete depths throughout the mantle (even-degree coefficients only). Dark shades indicate regions of higher than average velocities and light shades indicate slower than average regions. The scale for the maps is indicated at each depth. Coastlines have been superimposed for reference.

the μ and *S*-velocity models and between the κ and bulk sound velocity models are generally high. However, correlations drop near the CMB, suggesting that the density model in the lowermost mantle has different characteristics.

Finally, we present the first seismologically constrained whole-mantle density model (Fig. 13). The amplitude of density heterogeneity is relatively small near the surface and the CMB but is compatible with the 3-D velocity models in the mid-mantle. The pattern of density variations at 1300 km depth is most affected by the addition of the free-air gravity anomaly

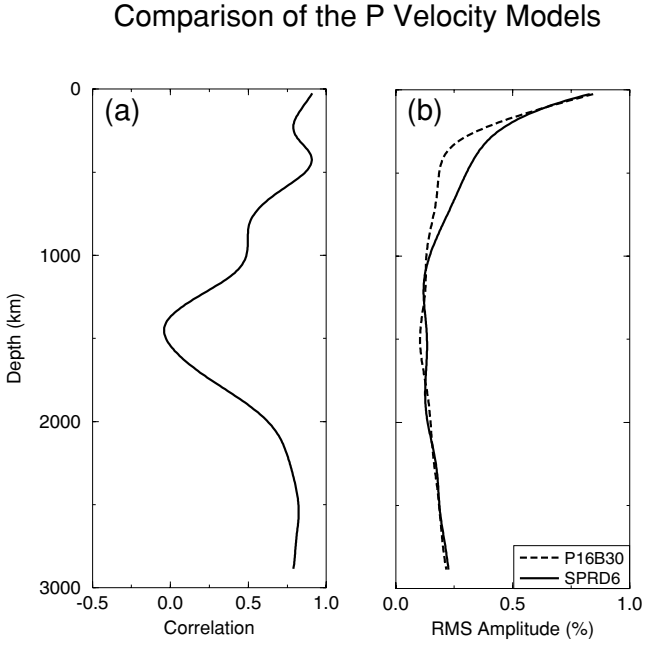

Figure 7. (a) Correlation between the *P* model of SPRD6e and P16B30 as a function of depth (even-degree coefficients). Poorer correlation is observed in the mid-mantle. (b) Rms amplitudes of the *P* part of SPRD6e and P16B30 as a function of depth (even-degree coefficients). The solid line is SPRD6e and the dashed line is P16B30.

constraint. This has been noted earlier in Forte *et al.* (1994) when geoid coefficients were combined with *S*-wave data to constrain a shear velocity model.

The density model beneath 1800 km depth shows little or no resemblance to the *S*- or *P*-velocity models. In fact, the correlation between density and seismic velocities approaches

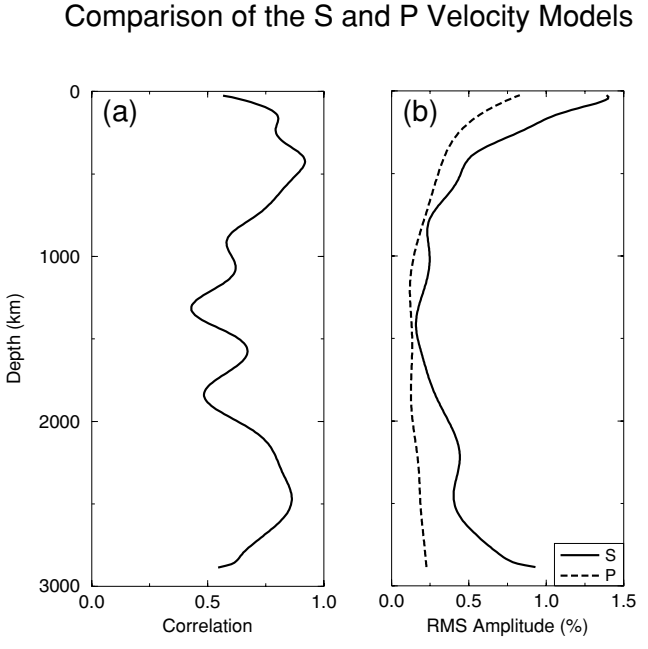

Figure 8. (a) Correlation between the even-degree part of the *S* and *P* parts of SPRD6e as a function of depth. (b) *S* and *P* rms amplitude as a function of depth (even degrees). The solid curve is the *S* model and the dashed curve is the *P* model.

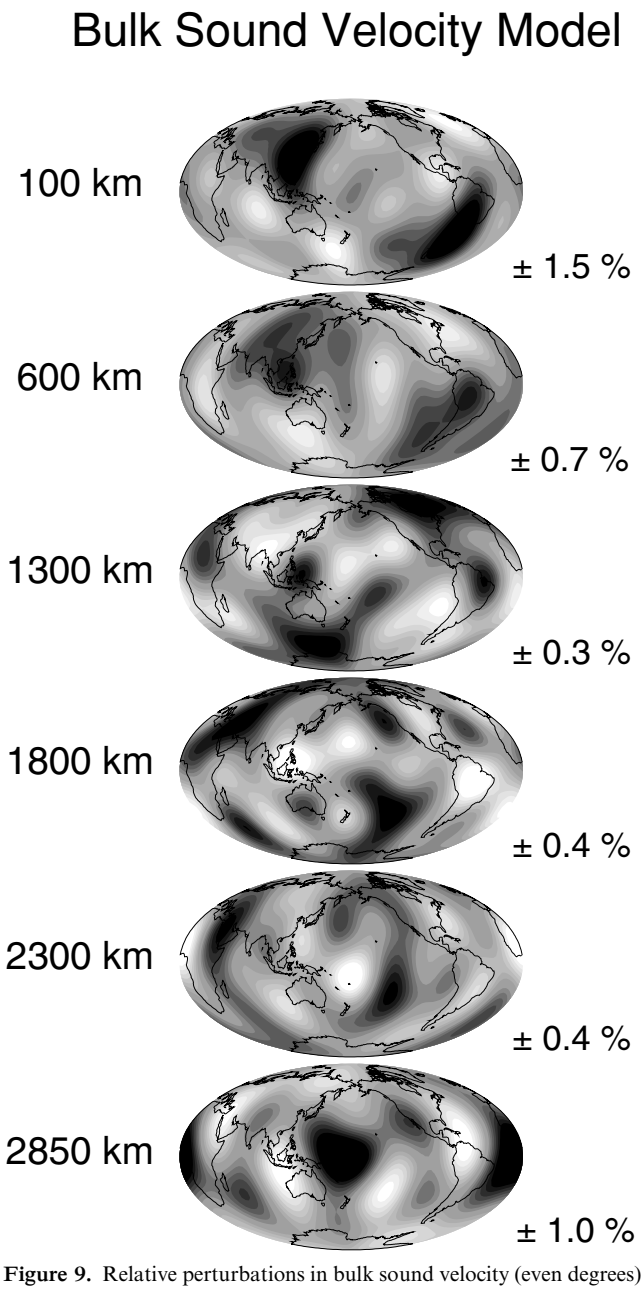

Figure 9. Relative perturbations in bulk sound velocity (even degrees) at six discrete depths. Dark regions indicate areas where the velocity is higher than average and light regions are areas with slower than average velocity. The scale of the maps is indicated at each depth and coastlines have been superimposed for reference.

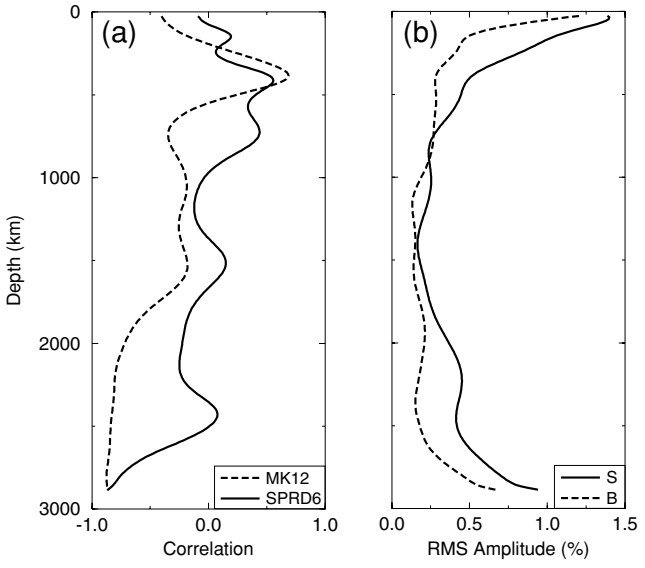

Figure 10. (a) Correlation between the shear and bulk sound (B) velocity models from our normal-mode inversion (solid line) and the body wave inversion by Su & Dziewonski (1997) (dashed line). This correlation plot is calculated using only the even-degree coefficients. (b) Rms amplitudes of shear velocity (solid line) and bulk sound velocity (dashed line) as a function of depth (even degrees only).

zero as the depth increases towards the CMB (Fig. 14a). Near the CMB, dense regions roughly correspond to the locations of slow shear velocity anomalies, which are traditionally interpreted as mantle upwellings. In contrast, density is reasonably well correlated with the bulk sound velocity anomalies (Fig. 15).

5.3 Topographic models

In Fig. 16(a), dynamic topography obtained from our normal-mode and free-air gravity anomaly inversion is plotted. Our dynamic topography is the undulation of the free surface without contributions due to the isostatically compensated crust. It is not related to the continent–ridge distribution as in the Forte & Woodward (1997) model. As we discuss in the following section, this boundary is the least constrained of all our models. Although our constraints on the 660 are better than those on the 410, the sensitivity to this discontinuity is still poor. Consequently, we have forced the model to be close to Gu *et al.* (1998) (Fig. 16b). The topographic model of the CMB (Fig. 16c) is the best constrained of all the boundaries. Interestingly, although models of the CMB are dominated by power in degree 2, our model has the most power in degree 2 order 1, whereas models by Morelli & Dziewonski (1987) and Forte *et al.* (1995) have leading power in the second order.

6 ROBUSTNESS OF THE MODELS

As part of this study, we performed many tests related to data quality and model resolution. In the interest of space, results from a limited number of tests may be viewed online at http://www.seismology.harvard.edu/projects/modes/. In this section, we refer to these supplementary figures. We will discuss resolution and uniqueness of the SPRD6e inversion in this section, focusing on the density model.

The pattern of density heterogeneity we obtain from the mode data alone is stable, but has a range of amplitudes that satisfy the data equally well. Inclusion of the free-air gravity anomaly narrows the amplitude range of the density heterogeneity and slightly modifies its pattern in the mid-mantle. At the same time, it introduces a trade-off between density heterogeneity and topography on boundaries. Because of this highly

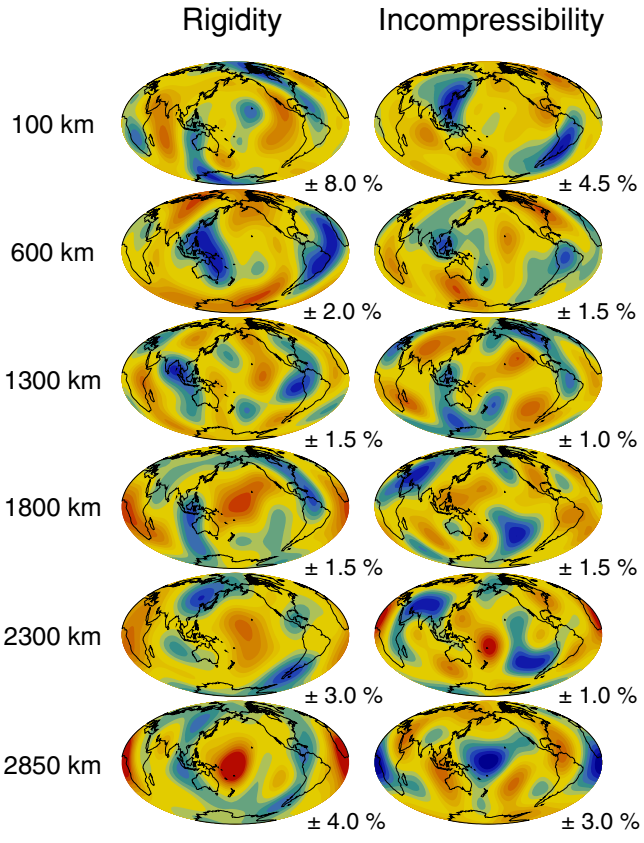

Figure 11. Relative perturbations in rigidity or shear modulus (left column) and incompressibility or adiabatic bulk modulus (right column) at six discrete depths (even-degree coefficients). Blue colours indicate regions of higher than average values and red colours indicate lower than average regions. The model of rigidity is very similar to that of shear velocity (Fig. 4), and incompressibility is also highly correlated with the bulk sound model (Fig. 9).

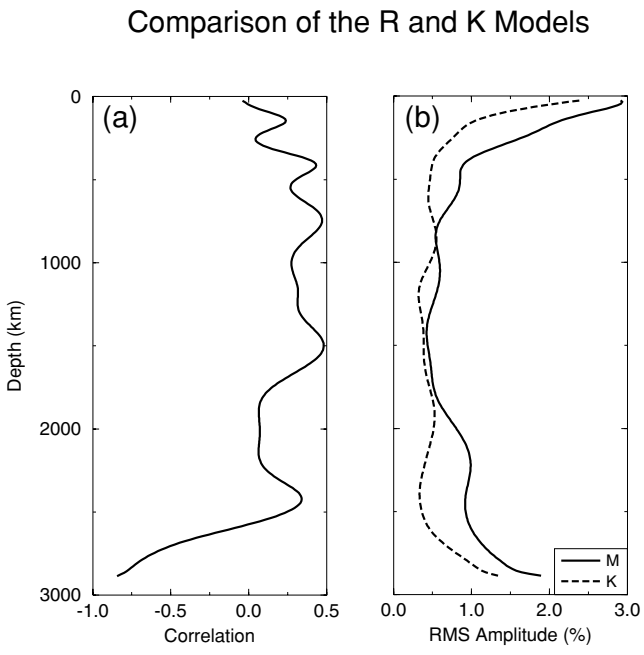

Figure 12. (a) Correlation between the even-degree part of the rigidity (M) and incompressibility (K) models as a function of depth. (b) Rms amplitudes of the rigidity and incompressibility parts of SBRD6e as a function of depth (even degrees). The solid line is the rms amplitude of rigidity and the dashed line is that of incompressibility.

non-unique dependence of the gravity anomaly on structure in density and boundary topography, we damp the inversion such that the resulting models are very close to those obtained from an inversion based only upon normal-mode data.

To determine the resolution of our density model, we first investigate its dependence on the starting model. Resovsky & Ritzwoller (1999b) found that *a priori* starting models influence the resulting density model greatly. We vary the scaling value for the S to density conversion, v_ρ, and find that the density models resulting from the inversions are consistent with one another; this includes starting with a zero-density model. Density is also relatively insensitive to the P starting model (supplementary Fig. 2). The inverted density model can be influenced by the parametrization of the inversion due to the effects of damping. However, density models obtained from three inversions with different parametrizations are highly compatible with one another (Fig. 3), indicating that the dependence of density on parametrization is limited.

We also investigate the results of inversions for density with and without boundary topography (supplementary Fig. 4). To do this, we must remove the free-air gravity constraint from our inversions, since it cannot be modelled without boundary topography. Therefore, we perform two inversions with only

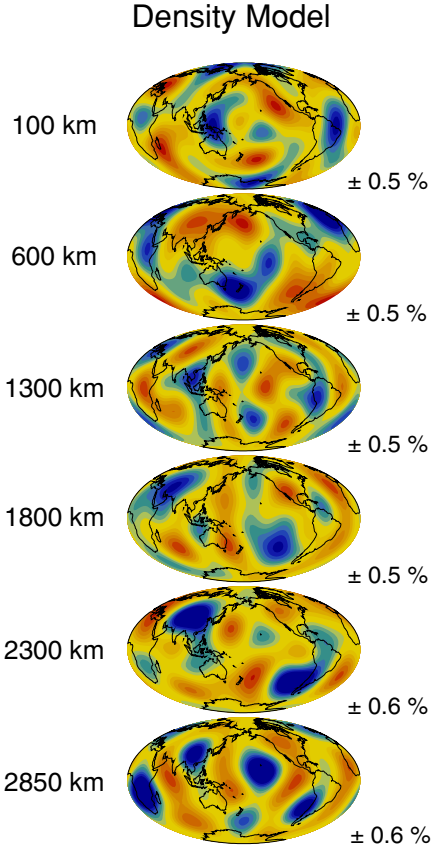

Figure 13. Relative perturbations in density at six discrete depths using only the even-degree coefficients. Blue regions denote higher than average density and red regions denote lower than average density. The scale of the maps is indicated at each depth. Coastlines have been superimposed for reference.

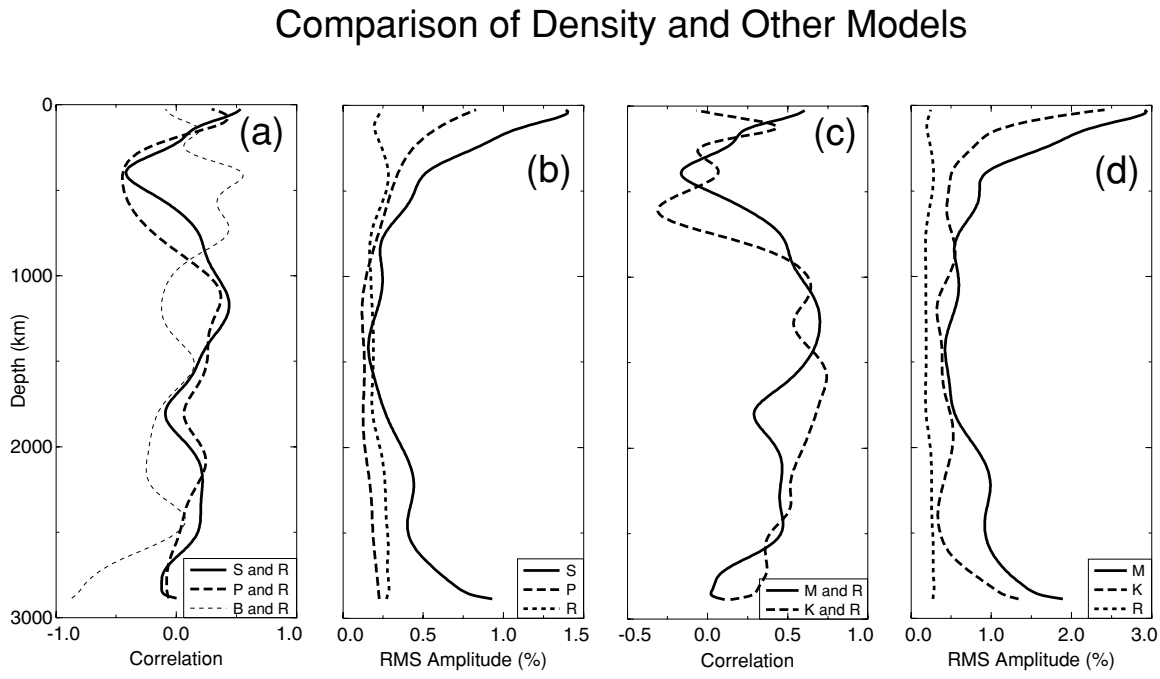

Figure 14. These curves are calculated using only the even degrees. The significant correlation at the 95 per cent confidence level is 0.32. R represents the density model. (a) Correlation between the density model of SPRD6e and *S* velocity (solid line), *P* velocity (dashed line) and bulk sound velocity (dotted line) as a function of depth. (b) Rms amplitude comparison of *S* velocity (solid line), *P* velocity (dashed line) and density (dotted line) heterogeneity as a function of depth. (c) Correlation between density and rigidity (solid line) and density and incompressibility (dashed line) as a function of depth. (d) Rms amplitude comparison of rigidity (solid line), incompressibility (dashed line) and density (dotted line) as a function of depth.

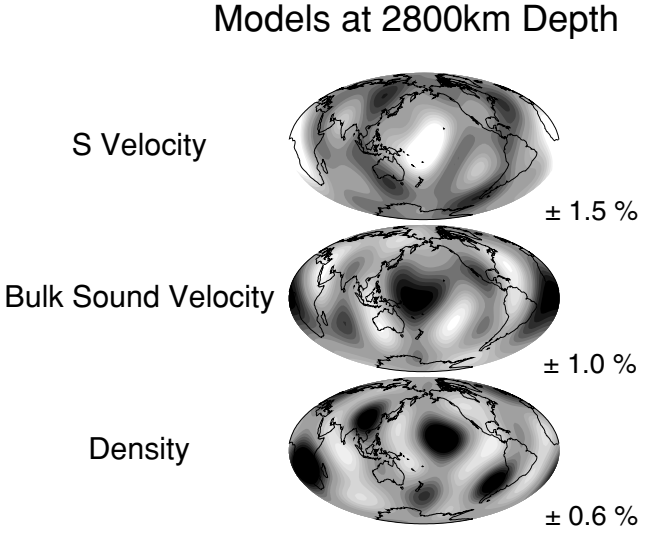

Figure 15. Map views of the even-degree part of shear velocity, bulk sound velocity and density from an inversion with these model parameters (model SBRD6e). The shading is the same as in previous figures. Note the strong anti-correlation between shear and bulk sound velocity.

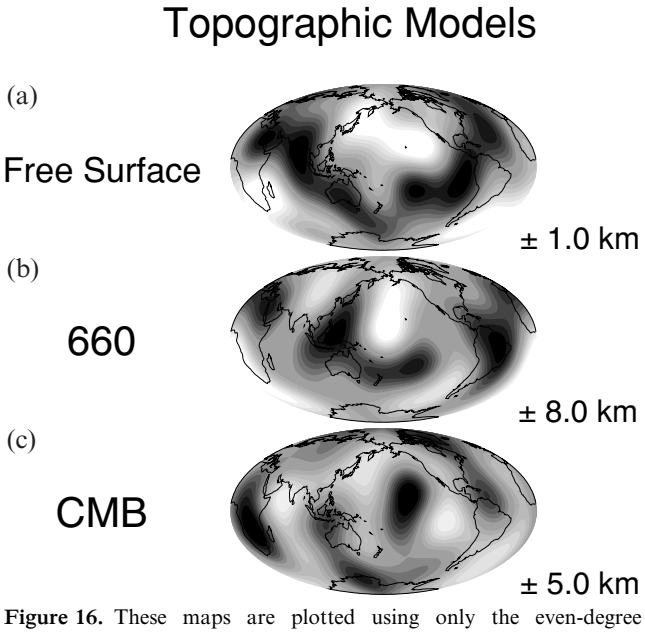

Figure 16. These maps are plotted using only the even-degree coefficients. (a) Map of dynamic free-surface topography. The scale for the map is indicated beside the model. Dark shades indicate areas of depression and light shades indicate areas of elevation. Coastlines have been superimposed for reference. (b) Map of 660 topography. The shading is the same as in (a), but note the enhanced scale. (c) Map of CMB topography.

normal-mode data. In the first inversion, we assume that topography on boundaries is negligible and invert only for S velocity, P velocity and density. In the second inversion we determine S and P velocities, density and boundary topography. The models resulting from the two inversions are highly correlated. We find that there is a trade-off between density and boundary topography, but this does not significantly influence the pattern of density heterogeneity. Introduction of topography, however, does reduce the amplitude of the density model near a boundary (supplementary Fig. 4b).

In supplementary Fig. 5(c), resolution in the lower mantle is investigated by a resolution test with input models peaked at 2700 km depth. In this test, density is the best resolved of the three models. The S velocity is also well resolved, but the recovery of the P model is poor. Supplementary Fig. 6(c) illustrates the components of 'true' Earth structure that contribute to produce a spike at 2800 km depth in model SPRD6e, a Backus–Gilbert test. In supplementary Fig. 7, checkerboard resolution tests are plotted for different input models. These tests show that the density model is not a result of contamination from the S- or P-velocity structure as concluded in Kuo & Romanowicz (1999). Density consistently shows better recovery than the other two models and the effect of strong damping on higher-degree structure manifests itself in terms of a poorer resolution. The S velocity is also well resolved, but the recovery of the P model is relatively poor.

In Fig. 17, we show our resolution matrix for degree 2 structure. Because our damping does not depend upon angular order, the resolution matrix for $s=2$, $t=1$ is virtually identical to the rest of the degree 2 components. This figure illustrates that high-order Chebyshev polynomials are very poorly resolved and that of the three volumetric models, the P-velocity model is the least constrained, as discussed previously.

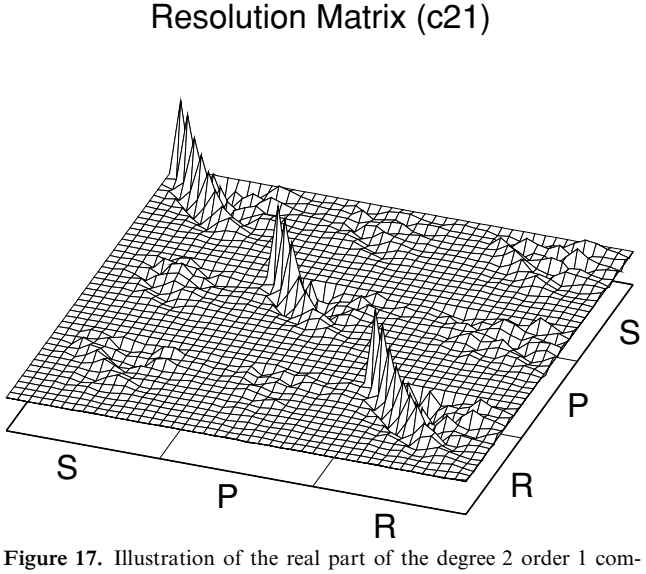

Figure 17. Illustration of the real part of the degree 2 order 1 component of the resolution matrix. The model coefficients are ordered such that the S-velocity model coefficients are at the far left corner, those for P velocity are in the middle, and those for density are at the front right corner. In each part, there are contributions from 14 radial basis functions, which are in increasing order from the back to the front. Because the damping used in the inversion does not depend upon the angular order, other degree 2 components have resolution matrices that are virtually identical to the one plotted here. Ideally, the resolution matrix should be the unit matrix. We see that off-diagonal terms are relatively small, and that higher-order Chebyshev polynomials are not well resolved due to strong damping.

The models of boundary topography are poorly resolved in our inversions, and of the three topographic models the free surface is the least constrained. There is a wide range of acceptable amplitudes with very minor amplitude changes to the 3-D density model, and little change in the free-air gravity fit. In order to obtain reasonable topography on the free surface, the amplitude of our dynamic topography has been damped to a size that is between the observed dynamic topography (Cazenave *et al.* 1989; Gurnis 1990) and that predicted from mantle-flow calculations (Forte & Woodward 1997). The 660 model has also been damped strongly towards the model of Gu *et al.* (1998). Finally, we require the CMB to have an overall amplitude that is in agreement with that of Morelli & Dziewonski (1987). Degree 2 structure of the CMB is resolved reasonably well, but higher degrees are not (supplementary Fig. 8).

Topography could exist on a mid-mantle boundary (e.g. Kawakatsu & Niu 1994; Wen & Anderson 1997) or on discontinuities within D″ (e.g. Lay *et al.* 1998). Because most modes have negligible sensitivity to undulations on internal discontinuities, these additional boundaries are unlikely to alter volumetric models significantly. They are, however, important when calculating the gravity anomaly, but, as mentioned before, this mainly alters the amplitude of our density model and not its pattern.

The statistical validity of the increased number of model parameters from a shear-velocity-only inversion (S6e) to model SPRD6e is investigated in Table 2. The values of χ^2/N_e and $\chi^2/(N_e-M_e)$, where N_e and M_e are the number of even-degree data and model parameters, respectively, are monitored as the number of model parameters is increased. Changes in

Table 2. Comparison of statistical results for a variety of models and radial parametrizations. In model S6e, we determine lateral variations in S velocity up to degree 6, and assume that lateral variations in P velocity and density are proportional to the S-velocity variations by constant scaling factors of 0.55 and 0.2, respectively. In model SP6e, we invert for independent lateral variations in S and P velocity, but assume that the density model is proportional to the S model. These two inversions use only the mode data. The third inversion, model SPRD6e, allows for independent lateral variations in S velocity, P velocity and density, and additional variations in topography on the free surface, the 660 and the CMB. This inversion includes constraints imposed by the free-air gravity anomaly. K13 indicates that models are expanded radially in Chebyshev polynomials up to order 13 (overparametrized inversion), and K7 models use Chebyshev polynomials up to order 7.

Model	Variance reduction (per cent)	χ^2/N_e	$\chi^2/(N_e-M_e)$
S6e (K13)	89.4	2.7	3.1
SP6e (K13)	90.3	2.5	3.3
SPRD6e (K13)	92.0	2.0	3.5
S6e (K7)	88.1	3.0	3.2
SP6e (K7)	90.1	2.5	2.9
SPRD6e (K7)	91.7	2.1	2.8

$\chi^2/(N_e - M_e)$ indicate whether the increase in the number of model parameters is warranted by the data. This test is not useful when the models are overparametrized, as in inversions with Chebyshev polynomials up to order 13. We prefer to overparametrize our models and damp higher-order polynomials more strongly, rather than parametrizing the models with lesser degrees of freedom. To determine the number of radial parameters that can be resolved by the data, we decrease the Chebyshev polynomial order until we observe an effect on χ^2/N_e; this occurs at about order 7. When the models are expanded radially up to order 7, $\chi^2/(N_e - M_e)$ improves with the addition of P, and again when density and boundary topography are added. We note that error estimates of splitting coefficients only affect the values of $\chi^2/(N_e - M_e)$ and not its relative changes. Masters *et al.* (2000a) found that the fit to their data set did not improve when an independent density model was allowed for in their inversions, leading them to conclude that density inversions are premature.

Inversions using a cubic b-spline radial basis (de Boor 1978; Lancaster & Salkauskas 1990) produce models in which the main features agree well with those obtained using a Chebyshev polynomial radial basis (supplementary Fig. 14). Therefore, the dependence of the models on the radial basis is small. However, note that the power in the b-spline model near the surface and at the CMB is smaller than in the Chebyshev polynomial model. The reason for this is that the Chebyshev polynomials change rapidly near these boundaries, and the 14 equally spaced b-splines cannot accommodate such a rapid change. This may mean that the Chebyshev density model overestimates the rms near these two boundaries or an underestimation by the b-spline density model.

We have performed inversions in which various levels of random noise were added to the splitting-function coefficients to investigate the effects of data quality (supplementary Fig. 10). If the data set is of insufficient quality to determine independent lateral variations in density, as suggested by Masters *et al.* (2000a,b), inverted density models should be significantly affected by the addition of random noise. We find, however, that the resulting models are highly consistent with our original models, indicating that the data quantity and quality are sufficient to constrain density heterogeneity, even with substantial uncertainties in the splitting functions.

To demonstrate further that our results are robust, we divide our data set into two subsets. The first subset consists of data from Resovsky & Ritzwoller (1998) only, and the second consists of data from He & Tromp (1996). Strictly speaking, each subset is not large enough to perform an inversion for independent models of S velocity, P velocity and density; nevertheless, this experiment provides insight into the robustness of the density model. We obtain models that are consistent with the density model from the complete data set (supplementary Fig. 12). The dense anomalies near the CMB appear in each case.

To address the issue of anisotropy, we monitor the change in fit of individual modes as the number of degrees of freedom is increased (Fig. 2). The fit to the toroidal modes, which are not sensitive to P heterogeneity, is improved when lateral variations in P are introduced. To investigate the possibility of mapping anisotropic S-velocity structure into the P-velocity model, we have performed an inversion with only spheroidal modes. The resulting P and S models are highly consistent with models obtained based upon the entire data set (supplementary Fig. 13), suggesting that we are indeed modelling isotropic P and S heterogeneity, rather than an anisotropic signal. However, note that anisotropy is not fully explored in this study. Fig. 2 illustrates further that only density-sensitive spheroidal modes show significant improvements in fit when going from model SP6e to model SPRD6e.

These tests indicate that we are resolving the density structure of the mantle despite claims that the current data set is of insufficient quality to constrain density reliably (Kuo & Romanowicz 1999; Masters *et al.* 2000a,b).

7 SCALING RELATIONS

One of the applications of our laterally varying models of the mantle is to compare them with mineral physics predictions. A common practice is to compare seismically obtained scaling values relating two models, such as shear velocity and density, with values determined by theoretical calculations or experiments. Therefore, we will first estimate the proportionality between two 3-D models as a function of depth. The 1-D scaling relationship between shear velocity and density, $v_\rho(r)$, is particularly important because it is used in mantle-flow calculations such as modelling of the geoid and constraining the viscosity profile of the mantle. We then investigate laterally varying scaling ratios.

7.1 Radial scaling relationships

Mineral physicists determine depth-dependent relationships between various model parameters such as S and P velocity by assuming that variations are due to temperature. For example,

$$\left(\frac{\delta \ln \beta}{\delta \ln \alpha}\right)_P = \frac{\alpha}{\beta}\,\frac{(\partial\beta/\partial T)_P}{(\partial\alpha/\partial T)_P} \qquad \text{or} \qquad \left(\frac{\delta \ln \rho}{\delta \ln \beta}\right)_P = \frac{\beta}{\rho}\,\frac{(\partial\rho/\partial T)_P}{(\partial\beta/\partial T)_P},$$

where T denotes temperature, and the derivatives are determined at constant pressure P. However, this formulation neglects variations due to other factors such as composition, a phase change or partial melting. The validity of a purely thermal source of lateral variations is debatable, especially when the correlation between two models is low, and this may be the cause of discrepancies between seismic and mineral physics estimates.

Seismology has constrained the scaling relationship between S and P velocities by examining S- and P-wave station corrections (e.g. Souriau & Woodhouse 1985), comparing S and P rms amplitudes (e.g. Dziewonski & Woodhouse 1987; Ritzwoller & Lavely 1995) or jointly inverting for an S or a P model and a depth-dependent scaling parameter (Bolton 1996; Robertson & Woodhouse 1996). These methods rely on a perfect correlation between S and P heterogeneity, which we have shown to be a questionable assumption, especially in the lower mantle (Fig. 8a).

Rather than determining scaling relationships based upon rms ratios, we apply a least-squares fitting technique (York 1969). At a given depth, we look for a constant value, v, which best relates model X to model Y by minimizing the objective

function

$$f(v) = \sum_i \frac{(y_i - vx_i)^2}{(\Delta y)_i^2 + v^2(\Delta x)_i^2} \,. \tag{11}$$

The summation, i, is over all coefficients, and x_i and y_i are the coefficients of models X and Y with their associated uncertainties $(\Delta x)_i$ and $(\Delta y)_i$, respectively. This is the least-squares fit of a straight line to coefficients with uncertainties in both the x- and y-directions. When two models are perfectly correlated, the coefficients lie on a straight line. However, when the two models are poorly correlated the coefficients x_i and y_i are randomly distributed and the best-fitting slope is either zero or infinity. The derivation of eq. (11) is discussed in Taylor (1997).

The uncertainties we assign to each coefficient in this analysis are not taken from the diagonal elements of the covariance matrix. In a damped least-squares inversion, such as we use to obtain our models, it is difficult, if not impossible, to obtain realistic error estimates. Strongly damped parameters with large elements of the damping matrix **D** are confined to a small portion of the model space around the starting model. Because of this confinement, these parameters cannot vary much from their starting values, and hence the uncertainty determined from the covariance matrix (eq. 7) is very small. In our calculations of scaling relations, we assign error estimates based upon data abundance, that is, we let the estimated uncertainty be inversely proportional to the square root of the number of observations at a given degree and order.

In Fig. 18(a), the depth-dependent scaling parameter between the S and P models obtained through the regression analysis is shown together with seismic estimates from Bolton (1996) and Robertson & Woodhouse (1996), as well as an estimate from mineral physics (Karato 1993). Seismically obtained values for the scaling between S and P velocities are highly consistent with one another. However, our result and the profile determined by Bolton differ in the upper mantle, even though the correlation between the S and P models is relatively high (Fig. 8a). Other seismic studies, using data such as station corrections, indicate an upper mantle value of around 2 (e.g. Souriau & Woodhouse 1985), which is in good agreement with our result. This high value near the surface is usually attributed to the presence of large-scale partial melting. In the lower mantle, the values based upon laboratory measurements are typically around 1.7 (Agnon & Bukowinski 1990; Isaak *et al.* 1992). Seismically determined values are larger, and various mechanisms such as large-scale partial melting (Agnon & Bukowinski 1990; Isaak *et al.* 1992), compositional heterogeneity (Jeanloz & Knittle 1989; Jackson 1998) and a phase change (Yeganeh-Haeri *et al.* 1989) have been invoked to explain these values.

The least-squares regression is meaningless when the correlation between the two models is poor. Examples of this are the unreasonably large values around 1300 km and beneath 2500 km depth, where the correlation between the S- and P-velocity models is low (Fig. 8). Effects other than temperature variations may be important in such poorly correlated regions. The particularly large values near the CMB are due to the compounded effects of a poor correlation and an increasing rms amplitude ratio. Here, another unknown is the effect of anisotropy.

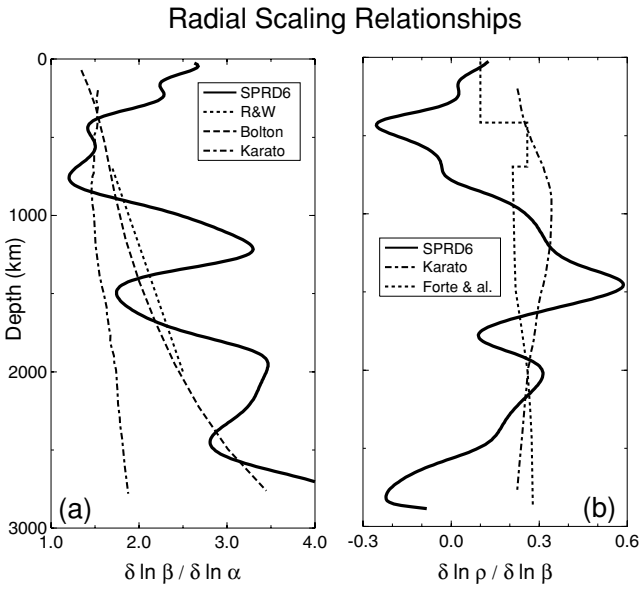

Figure 18. (a) Proportionality between the S and P models, $\delta \ln \beta / \delta \ln \alpha$, where β is the S velocity and α is the P velocity. The solid curve is the estimate based upon the SPRD6e inversion. The dashed curve represents the model from Robertson & Woodhouse (1996), the dotted curve is from Bolton (1996) and the dot-dashed curve is from Karato (1993). The former two curves are determined by inverting S- and P-wave data for S or P heterogeneity and a depth-dependent scaling relation, assuming a perfect correlation between the S and P models. The Robertson & Woodhouse model only spans depths between 700 and 2000 km. Karato's profile is based upon mineral physics estimates. (b) Proportionality between density and S velocity, $\delta \ln \rho / \delta \ln \beta$, where ρ is the density. The solid curve is obtained from the S-velocity and density parts of SPRD6e, the dot-dashed curve is from Karato (1993) and the dotted curve is from Forte *et al.* (1994).

In Fig. 18(b), we compare our result based upon the 3-D density and shear velocity models to those of Karato (1993) and Forte *et al.* (1994). The profile by Karato is calculated using thermal derivatives based upon an experimentally determined activation energy and considering the effects of attenuation. On the other hand, the profile by Forte *et al.* has been obtained through an inversion of geoid and seismic observations. The profiles are in reasonable agreement in the mid-mantle where the correlation between density and shear velocity is relatively high. Differences between the profiles occur around the transition zone and in the lowermost mantle, and the scaling values we obtain in these regions are often negative. Mineral physics estimates of the scaling value between density and shear velocity lie between 0.2 and 0.4 (Anderson *et al.* 1968; Anderson 1987, 1989). Our profile $\pm$ one error bar includes this range almost throughout the mantle. However, considering the low correlation between density and shear velocity, it is not obvious how useful this radially dependent scaling relation is in characterizing the density structure of the mantle.

7.2 Laterally varying scaling ratios

In the previous section we found that depth-dependent scaling relations are not very useful when models are poorly correlated. Alternatively, one may calculate lateral variations in the scaling

ratio to identify anomalous regions. For example, Bolton (1996) noted that beneath the central Pacific, the ratio of S to P velocity is anomalously high in the lowermost mantle. There is, however, a problem. The 3-D models represent perturbations from the 1-D reference earth model: there are inevitably regions where the model values are zero, resulting in singularities when a ratio is calculated. To avoid these singularities, we determine lateral variations in the scaling ratio by combining the 3-D models with the reference 1-D model to obtain the absolute values of velocity and density.

In Fig. 19, variations in the ratio of S to P velocity and density to S velocity are plotted at six discrete depths. The laterally varying S-to-P ratio shows low-degree heterogeneity in the upper and lowermost mantle, but the mid-mantle is characterized by higher-degree structure. Near the CMB, the pattern is similar to that of the S-velocity model.

The ratio of density to S velocity is generally dominated by the pattern of the S anomaly since lateral variations in density are weaker than those in S (Fig. 14b). Deviations from S patterns are observed when the correlation between density and S-velocity models is low, such as in the transition zone and near the CMB.

Another parameter that may be of interest is Poisson's ratio. This material characteristic describes the ratio of thinning to elongation, or thickening to contraction, and varies between 0.1 and 0.4 for different rocks (Turcotte & Schubert 1982). In terms of rigidity μ and incompressibility κ, Poisson's ratio σ is given by $\sigma=(3\kappa-2\mu)/(6\kappa+2\mu)$. In Fig. 20, Poisson's ratio obtained from the rigidity and incompressibility models of MKRD6e is plotted at six discrete depths. The plots are highly anti-correlated with those of the S-to-P velocity ratio. This is to be expected since Poisson's ratio can be written in terms of the ratio of seismic velocities as $\sigma=[(\alpha/\beta)^2-2]/[2(\alpha/\beta)^2-2]$.

8 DISCUSSION AND CONCLUSIONS

We have demonstrated that normal-mode data, with additional constraints from the Earth's gravity field, can constrain independent even-degree lateral variations in S velocity, P velocity and density, or, alternatively, rigidity, incompressibility and density. Our velocity models are consistent with existing traveltime models, with the exception of the mid-mantle. Such disagreements exist between body wave models and are mainly due to a relatively small rms amplitude in the mid-mantle range. Normal modes provide useful constraints in this region because some modes are particularly sensitive to mid-mantle

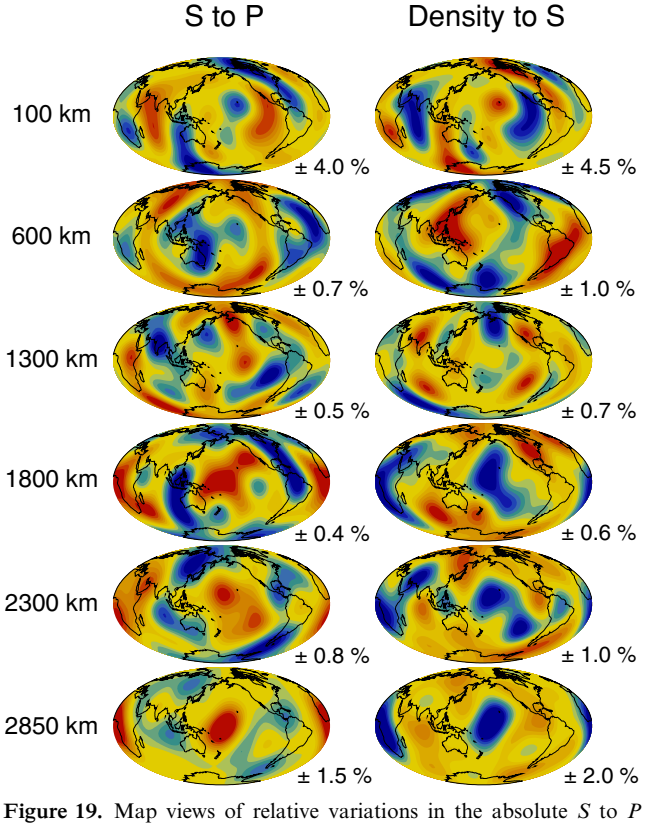

Figure 19. Map views of relative variations in the absolute S to P velocity ratio (left column) and the absolute density to S velocity ratio (right column). Red colours indicate higher than average anomalies and blue colours indicate lower than average ratios. The scale of the colour scheme is indicated at each depth. Coastlines have been superimposed for reference.

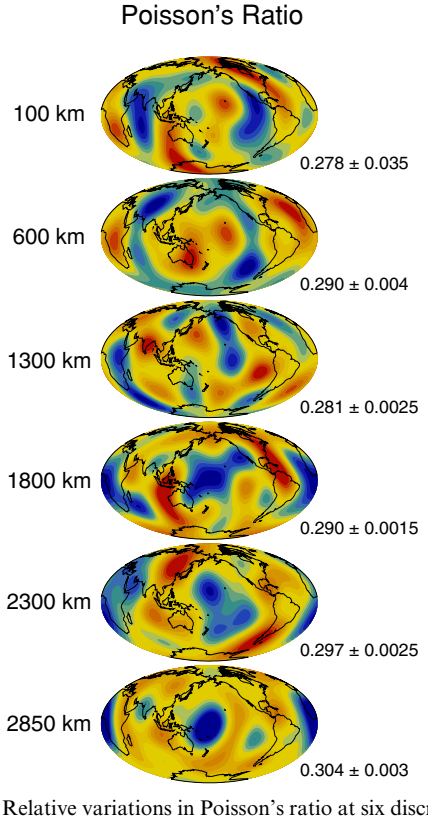

Figure 20. Relative variations in Poisson's ratio at six discrete depths. The colour scheme is the same as in Fig. 19 and the scale for each map is shown along with the reference value at each depth. The slow S-velocity anomaly beneath the Pacific appears as a strong positive Poisson's ratio anomaly almost throughout the lower mantle, but the African anomaly is much weaker.

structure. The models of rigidity and incompressibility are well correlated with models of shear and bulk sound velocity, respectively.

The resolvability of density structure using normal-mode data has been questioned in several studies. Resovsky & Ritzwoller (1999b) and Kuo & Romanowicz (1999) found that the density model strongly depends upon *a priori* assumptions. We show that our density model is relatively insensitive to the starting model and the model parametrization. Inversion for a density model is considered 'premature' by Masters *et al.* (2000a,b). With numerous resolution tests, including those with noise, using subsets of the data, and analysis of the resolution matrix, we believe that our density model is reliably constrained.

The rms amplitude of this model is almost constant throughout the mantle, with slight increases in the transition zone and near the CMB. In the transition zone the density model is significantly decorrelated from the velocity models, suggesting that lateral variations in this region are not entirely due to variations in temperature. Compositional variations in the transition zone have been suggested previously, for example, based upon the significant decorrelation between 410 topography and velocity at that depth (Flanagan & Shearer 1999). The most prominent features of our density model appear in the lowermost mantle, where high-density anomalies are at locations where slow velocity anomalies are observed. This is consistent with convection simulations where dense material piles up beneath upwellings because it is too heavy to be entrained in the uplift (Christensen 1984; Davies & Gurnis 1986; Hansen & Yuen 1988; Tackley 1998). Introduction of heavy core material into the mantle beneath upwellings can also produce such density anomalies (Knittle & Jeanloz 1991).

A further illustration of the nature of the lowermost mantle is obtained by examining shear velocity, bulk sound velocity and density heterogeneity near the CMB. Our results confirm earlier observations of an anti-correlation between shear and bulk sound velocity (Su & Dziewonski 1997; Masters *et al.* 2000c), and, combined with the regional anti-correlation between shear velocity and density, strongly suggest that compositional, as well as thermal, heterogeneity is required to explain lateral variations in the lowermost mantle.

We also present several depth-dependent scaling relations between the models obtained from our inversions. Instead of assuming a perfect correlation between models, we perform a least-squares regression. The relations determined using this approach agree well with previous studies when the models are highly correlated. However, when the correlation of the models is poor, the depth-dependent relationships do not provide meaningful information. Therefore, we have also determined laterally varying scaling ratios using absolute values instead of relative perturbations.

ACKNOWLEDGMENTS

We wish to thank R. J. O'Connell, Svetlana Panasyuk, Jerry X. Mitrovica, Hendrik Jan van Heijst and Guy Masters for numerous discussions and suggestions. We also thank Jeffrey Park for a constructive review. This research was supported by the David and Lucile Packard Foundation. MI was also supported by a Natural Sciences and Engineering Research Council of Canada Postgraduate Scholarship.

REFERENCES

Agnon, A. & Bukowinski, M.S.T., 1990. δ_S at high pressure and $d \ln V_s / d \ln V_p$ in the lower mantle, *Geophys. Res. Lett.,* **17,** 1149–1152.

Anderson, D.L., 1987. A seismic equation of state II. Shear properties and thermodynamics of the lower mantle, *Phys. Earth planet. Inter.,* **45,** 307–323.

Anderson, D.L., 1989. *Theory of the Earth,* Blackwell, Oxford.

Anderson, O.L., Schreiber, E., Liebermann, R.C. & Soga, N., 1968. Some elastic constant data on minerals relevant to geophysics, *Rev. Geophys.,* **6,** 491–524.

Backus, G. & Gilbert, F., 1968. The resolving power of gross Earth data, *Geophys. J. R. astr. Soc.,* **16,** 169–205.

Bolton, H., 1996. Long period travel times and the structure of the mantle, *PhD thesis,* University of California, San Diego.

Cazenave, A., Souriau, A. & Dominh, K., 1989. Global coupling of Earth surface topography with hotspots, geoid and mantle, *Nature,* **340,** 54–57.

Christensen, U., 1984. Instability of a hot boundary layer and initiation of thermo-chemical plumes, *Ann. Geophys.,* **2,** 311–320.

Dahlen, F.A. & Tromp, J., 1998. *Theoretical Global Seismology,* Princeton University Press, Princeton, NJ.

Davies, G.F. & Gurnis, M., 1986. Interaction of mantle dregs with convection: lateral heterogeneity at the core-mantle boundary, *Geophys. Res. Lett.,* **13,** 1517–1520.

de Boor C., 1978., *A Practical Guide to Splines,* Springer Verlag, New York.

Dziewonski, A.M. & Anderson, D.L., 1981. Preliminary reference Earth model, *Phys. Earth planet. Inter.,* **25,** 297–356.

Dziewonski, A.M. & Woodhouse, J.H., 1987. Global images of the Earth's interior, *Science,* **236,** 37–48.

Dziewonski, A.M., Liu, X.-F. & Su, W.-J., 1997. Lateral heterogeneity in the lowermost mantle, in *Earth's Deep Interior*, pp. 11–50., ed. Crossley, D.J., Gordon and Breach, Amsterdam.

Edmonds, A.R., 1960. *Angular Momentum in Quantum Mechanics.,* Princeton University Press, Princeton, NJ.

Flanagan, M.P. & Shearer, P.M., 1998. Global mapping of topography on transition zone velocity discontinuities by stacking *SS* precursors, *J. geophys. Res.,* **103,** 2673–2692.

Flanagan, M.P. & Shearer, P.M., 1999. A map of topography on the 410-km discontinuity from PP precursors, *Geophys. Res. Lett.,* **26,** 549–552.

Forte, A.M. & Peltier, W.R., 1987. Plate tectonics and aspherical earth structure: the importance of poloidal-toroidal coupling, *J. geophys. Res.,* **92,** 3645–3679.

Forte, A.M. & Woodward, R.L., 1997. Seismic-geodynamic constraints on three-dimensional structure, vertical flow, and heat transfer in the mantle, *J. geophys. Res.,* **102,** 17 981–17 994.

Forte, A.M., Woodward, R.L. & Dziewonski, A.M., 1994. Joint inversions of seismic and geodynamic data for models of three-dimensional mantle heterogeneity, *J. geophys. Res.,* **99,** 21 857–21 877.

Forte, A.M., Dziewonski, A.M. & O'Connell, R.J., 1995. Continent-ocean chemical heterogeneity in the mantle based on seismic tomography, *Science,* **268,** 386–388.

Forte, A.M., Mitrovica, J.X. & Woodward, R.L., 1995. Seismic-geodynamic determination of the origin of excess ellipticity of the core-mantle boundary, *Geophys. Res. Lett.,* **22,** 1013–1016.

Giardini, D., Li, X.-D. & Woodhouse, J.H., 1987. Three-dimensional structure of the Earth from splitting in free-oscillation spectra, *Nature,* **325,** 405–411.

Giardini, D., Li, X.-D. & Woodhouse, J.H., 1988. Splitting functions of long-period normal modes of the Earth, *J. geophys. Res.,* **93,** 13 716–13 742.

Gu, Y., Dziewonski, A.M. & Agee, C.B., 1998. Global de-correlation of the topography of transition zone discontinuities, *Earth planet. Sci. Lett.,* **157,** 57–67.

Gurnis, M., 1990. Bounds on global dynamic topography from Phanerozoic flooding of continental platforms, *Nature,* **344,** 754–756.

Gwinn, C.R., Herring, T.A. & Shapiro, I.I., 1986. Geodesy by radio interferometry: studies of the forced nutations of the Earth 2. Interpretation, *J. geophys. Res.,* **91,** 4755–4765.

Hager, B.H. & Clayton, R.W., 1989. Constraints on the structure of mantle convection using seismic observations, flow models, and the geoid, in *Mantle Convection: Plate Tectonics and Global Dynamics,* pp. 657–763, ed. Peltier, W.R., Gordon and Breach, Newark, NJ.

Hansen, U. & Yuen, D.A., 1988. Numerical simulations of thermal-chemical instabilities at the core-mantle boundary, *Nature,* **334,** 237–240.

He, X. & Tromp, J., 1996. Normal-mode constraints on the structure of the Earth, *J. geophys. Res.,* **101,** 20 053–20 082.

Isaak, D.G., Anderson, O.L. & Cohen, R.E., 1992. The relationship between shear and compressional velocities at high pressures: reconciliation of seismic tomography and mineral physics, *Geophys. Res. Lett.,* **19,** 741–744.

Ishii, M. & Tromp, J., 1999. Normal-mode and free-air gravity constraints on lateral variations in velocity and density of the Earth's mantle, *Science,* **285,** 1231–1236.

Jackson, I., 1998. Elasticity, composition and temperature of the Earth's lower mantle, *Geophys. J. Int.,* **134,** 291–311.

Jeanloz, R. & Knittle, E.B., 1989. Density and composition of the lower mantle, *Phil. Trans. R. Soc. Lond.,* A**328,** 377–389.

Karato, S., 1993. Importance of anelasticity in the interpretation of seismic tomography, *Geophys. Res. Lett.,* **20,** 1623–1626.

Kawakatsu, H. & Niu, F., 1994. Seismic evidence for a 920-km discontinuity in the mantle, *Nature,* **371,** 301–305.

Knittle, E. & Jeanloz, R., 1991. Earth's core-mantle boundary: results of experiments at high pressures and temperatures, *Science,* **251,** 1438–1443.

Kuo, C. & Romanowicz, B., 1999. Aspherical mantle structure in density and seismic velocity determined from free oscillation spectra, *EOS, Trans. Am. geophys. Un.,* **80,** F760.

Lancaster, P. & Salkauskas, K., 1990. *Curve and Surface Fitting,* Academic Press, San Diego.

Lay, T., Williams, Q., Garnero, E.J., Kellogg, L. & Wysession, M.E., 1998. Seismic wave anisotropy in the D'' region and its implications, in *The Core-Mantle Boundary Region, Geodynamics Series,* Vol. 28, pp. 299–318, eds Gurnis, M., Wysession, M.E., Knittle, E. & Buffett, B.A., American Geophysical Union, Washington, DC.

Lemoine, F.G., *et al.*, 1997. The development of the NASA GSFC and NIMA joint geopotential model, in *International Association of Geodesy Symposia,* Vol. 117, pp. 462–269, eds Segawa, J., Fujimoto, H. & Okubo, S., Springer-Verlag, Berlin.

Lemoine, F.G., Pavlis, N.K., Kenyon, S.C., Rapp, R.H., Pavlis, E.C. & Chao, B.F., 1998a. New high-resolution model developed for Earth's gravitational field, *EOS, Trans. Am. geophys. Un.,* **79,** 117–118.

Lemoine, F.G., *et al.*, 1998b. The development of the joint NASA GSFC and National Imagery and Mapping Agency (NIMA) geopotential model, EGM96, *NASA/TP-1998–206861.*

Li, X.-D., Giardini, D. & Woodhouse, J.H., 1991. Large-scale three-dimensional even-degree structure of the Earth from splitting of long-period normal modes, *J. geophys. Res.,* **96,** 551–577.

Lithgow-Bertelloni, C. & Richards, M.A., 1998. The dynamics of Cenozoic and Mesozoic plate motions, *Rev. Geophys.,* **36,** 27–78.

Masters, G., Laske, G. & Gilbert, F., 2000a. Matrix autoregressive analysis of free-oscillation coupling and splitting, *Geophys. J. Int.,* **143,** 478–489.

Masters, G., Laske, G. & Gilbert, F., 2000b. Large-scale Earth structure from analysis of free oscillation splitting and coupling, in *Problems in Geophysics for the New Millennium,* pp. 255–288, eds Boschi, E., Ekström, G. & Morelli, A., Editrice Compositori, Bologna.

Masters, G., Laske, G., Bolton, H. & Dziewonski, A.M., 2000c. The relative behavior of shear velocity, bulk sound speed, and compressional velocity in the mantle: implications for chemical and thermal structure, in *Earth's Deep Interior: Mineral Physics and Tomography From the Atomic to the Global Scale,* Geodynamic Ser., Vol. 117, pp. 63–87, eds Karato, S., Forte, A.M., Liebermann, R.C., Masters, G. & Stixrude, L., AGU, Washington DC.

Mooney, W.D., Laske, G. & Masters, T.G., 1998. Crust 5.1: a global crustal model at $5^\circ \times 5^\circ$, *J. geophys. Res.,* **103,** 727–747.

Morelli, A. & Dziewonski, A.M., 1987. Topography of the core-mantle boundary and lateral homogeneity of the liquid core, *Nature,* **325,** 678–683.

Nakiboglu, S.M., 1982. Hydrostatic theory of the Earth and its mechanical implications, *Phys. Earth planet. Inter.,* **28,** 302–311.

Resovsky, J.S. & Ritzwoller, M.H., 1995. Constraining odd-degree Earth structure with coupled free-oscillations, *Geophys. Res. Lett.,* **22,** 2301–2304.

Resovsky, J.S. & Ritzwoller, M.H., 1998. New constraints on deep Earth structure from generalized spectral fitting: application to free oscillations below 3 mHz, *J. geophys. Res.,* **103,** 783–810.

Resovsky, J.S. & Ritzwoller, M.H., 1999a. A degree 8 mantle shear velocity model from normal mode observations below 3 mHz, *J. geophys. Res.,* **104,** 993–1014.

Resovsky, J.S. & Ritzwoller, M.H., 1999b. Regularization uncertainty in density models estimated from normal mode data, *Geophys. Res. Lett.,* **26,** 2319–2322.

Ricard, Y., Richards, M., Lithgow-Bertelloni, C. & Le Stunff, Y., 1993. A geodynamic model of mantle density heterogeneity, *J. geophys. Res.,* **98,** 21 895–21 909.

Ritzwoller, M.H. & Lavely, E.M., 1995. Three-dimensional seismic models of the Earth's mantle, *Rev. Geophys.,* **33,** 1–66.

Ritzwoller, M.H. & Resovsky, J.S., 1995. The feasibility of normal mode constraints on higher degree structures, *Geophys. Res. Lett.,* **22,** 2305–2308.

Ritzwoller, M.H., Masters, G. & Gilbert, F., 1988. Constraining aspherical structure with low-degree interaction coefficients: application to uncoupled multiplets, *J. geophys. Res.,* **93,** 6369–6396.

Robertson, G.S. & Woodhouse, J.H., 1995. Evidence for proportionality of *P* and *S* heterogeneity in the lower mantle, *Geophys. J. Int.,* **123,** 85–116.

Robertson, G.S. & Woodhouse, J.H., 1996. Ratio of relative *S* to *P* velocity heterogeneity in the lower mantle, *J. geophys. Res.,* **101,** 20 041–20 052.

Souriau, A. & Woodhouse, J.H., 1985. A worldwide comparison of predicted S-wave delays from a three-dimensional upper mantle model with P-wave station corrections, *Phys. Earth planet. Inter.,* **39,** 75–88.

Su, W.-J., 1992. The three-dimensional shear-wave velocity structure of the Earth's mantle, *PhD thesis,* Harvard University, Cambridge, MA.

Su, W.-J. & Dziewonski, A.M., 1997. Simultaneous inversion for 3-D variations in shear and bulk velocity in the mantle, *Phys. Earth planet. Inter.,* **100,** 135–156.

Su, W.-J., Woodward, R.L. & Dziewonski, A.M., 1994. Degree-12 model of shear-velocity heterogeneity in the mantle, *J. geophys. Res.,* **99,** 6945–6980.

Tackley, P.J., 1998. Three-dimensional simulations of mantle convection with a thermo-chemical basal boundary layer: D''?, in *The Core-Mantle Boundary Region, Geodynamics Series,* Vol. 28, pp. 231–253, eds. Gurnis, M., Wysession, M.E., Knittle, E. & Buffett, B.A., American Geophysical Union, Washington DC.

Tanimoto, T., 1991. Waveform inversion for three-dimensional density and *S* wave structure, *J. geophys. Res.,* **96,** 8167–8189.

Taylor, J.R., 1997. *An Introduction to Error Analysis: The Study of Uncertainties in Physical Measurements,* 2nd edn, University Science Books, Sausalito, CA.

Tromp, J. & Zanzerkia, E., 1995. Toroidal splitting observations from the great 1994 Bolivia and Kuril Islands earthquakes, *Geophys. Res. Lett.,* **22,** 2297–2300.

Turcotte, D.L. & Schubert, G., 1982. *Geodynamics: Applications of Continuum Physics to Geological Problems,* John Wiley & Sons, New York.

Wen, L. & Anderson, D.L., 1997. Layered mantle convection: a model for geoid and topography, *Earth planet. Sci. Lett.,* **146,** 367–377.

Woodhouse, J.H., 1980. The coupling and attenuation of nearly resonant multiplets in the Earth's free oscillation spectrum, *Geophys. J. R. astr. Soc.,* **61,** 261–283.

Woodhouse, J.H. & Dahlen, F.A., 1978. The effect of a general aspherical perturbation on the free oscillations of the Earth, *Geophys. J. R. astr. Soc.,* **53,** 335–354.

Yeganeh-Haeri, A., Weidner, D.J. & Ito, E., 1989. Elasticity of $MgSiO_3$ in the perovskite structure, *Science,* **243,** 787–789.

York, D., 1969. Least squares fitting of a straight line with correlated errors, *Earth planet. Sci. Lett.,* **5,** 320–324.